CHALMERS
UNIVERSITY OF TECHNOLOGY

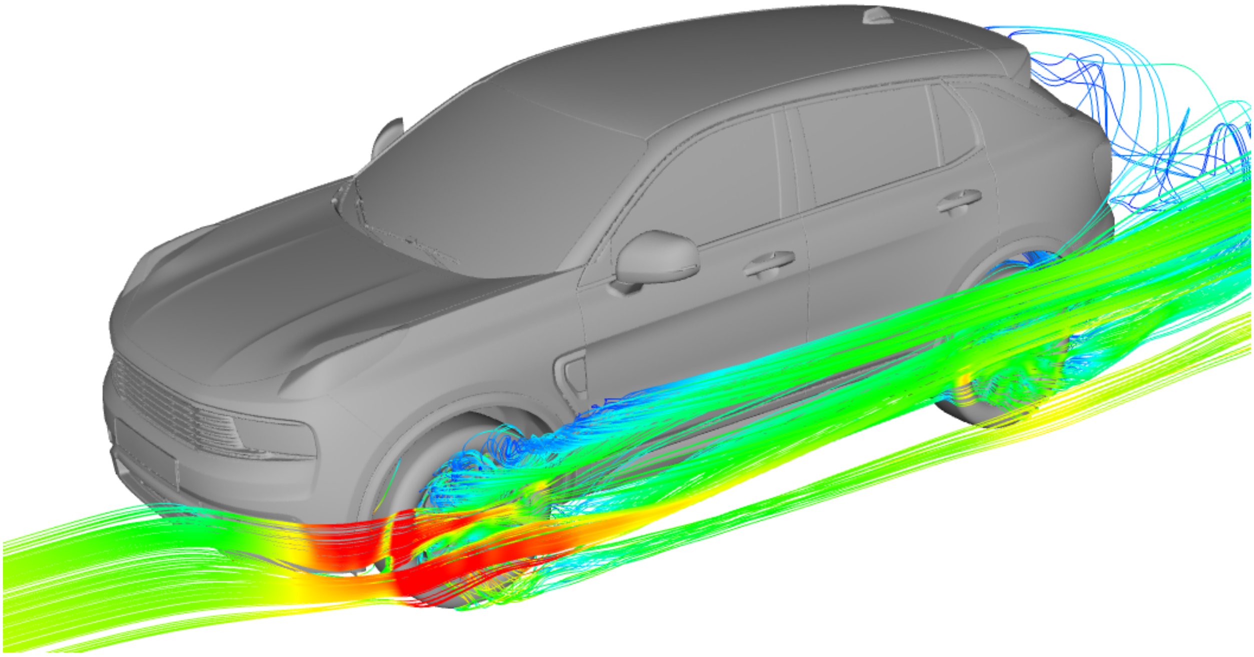

CFD Investigation on Sliding Mesh as a Method to Model Wheel Rotation

Implementation and Analysis on Different Rims

Master's thesis in Automotive Engineering

ANDRÉS CONTRERAS URIEGAS

Department of Mechanics and Maritime Sciences
CHALMERS UNIVERSITY OF TECHNOLOGY
Gothenburg, Sweden 2018

Master's thesis 2018

CFD Investigation on Sliding Mesh as a Method to Model Wheel Rotation

Implementation and Analysis on Different Rims

ANDRÉS CONTRERAS URIEGAS

CHALMERS
UNIVERSITY OF TECHNOLOGY

Department of Mechanics and Maritime Sciences
Division of Vehicle Engineering and Autonomous Systems
Chalmers University of Technology
Gothenburg, Sweden 2018

CFD Investigation on Sliding Mesh as a Method to Model Wheel Rotation
Implementation and Analysis on Different Rims
ANDRÉS CONTRERAS URIEGAS

Supervisor: Simone Sebben, Mechanics and Maritime Sciences
Advisor: Simon Lindberg, CEVT
Examiner: Simone Sebben, Mechanics and Maritime Sciences

Master's Thesis 2018:29
Department of Mechanics and Maritime Sciences
Division of Division of Vehicle Engineering and Autonomous Systems
Chalmers University of Technology and University of Gothenburg
SE-412 96 Gothenburg
Telephone +46 31 772 1000

Cover: Streamlines colored with the velocity magnitude constructed in Ensight showing the flow through the front and rear left wheels.

Typeset in LaTeX
Gothenburg, Sweden 2018

CFD Investigation on Sliding Mesh as a Method to Model Wheel Rotation
Implementation and Analysis on Different Rims
ANDRÉS CONTRERAS URIEGAS
Department of Mechanics and Maritime Sciences
Chalmers University of Technology

Abstract

Energy efficiency has become an incentive to further investigate sustainable alternatives for passenger mobility. Many engineering disciplines work continuously on minimizing the energy consumption of today's vehicles, being automotive aerodynamics one of them. In a moving car, aerodynamic drag becomes a dominant force after, approximately, 60 km/h and thus, it must be reduced to improve the vehicle's efficiency. In a passenger vehicle, the wheels and wheelhousings are a major contributor to the total drag of a vehicle. Hence, capturing the complex flow around the wheels is essential to improve on current solutions.

Computational Fluid Dynamics (CFD) simulations are widely used in the aerodynamic improvements of a vehicle. Traditionally, wheel rotation is modelled as a moving wall for the tyres and a Multiple Reference Frame (MRF) region for the rims. The MRF approach, is a simplified method that aims to model wheel rotation while keeping the computational resources low, and thus it is the common practice among carmakers. However, it is an approximation of the real motion of a wheel and it has a number of drawbacks. Alternatively, sliding mesh is an improved model that captures the true motion of a wheel and therefore it is considered to deliver an enhanced numerical solution compared to MRF.

This thesis aims at investigating the use of sliding mesh as a wheel rotation method and its correlation with wind tunnel tests. The method is evaluated on four different rims using the same vehicle as a baseline. All cases were solved in ANSYS Fluent 19.0 using a hybrid RANS-LES turbulence model. The investigation is carried out to enable a comparison against previously obtained wind tunnel force measurements. As part of the analysis, the results of interest are the drag, front-lift and rear-lift deltas (ΔC_D, ΔC_{FL} and ΔC_{RL}).

The implementation of the sliding mesh yielded comparable results to the ones obtained from the MRF simulations. However, the computation time increased significantly. Therefore restricting the number of cases performed in this study. In addition to the increased computational cost, the sliding mesh implementation failed to improve significantly over the MRF and thus putting in question a number of set parameters and boundary conditions applied. However, sliding mesh has shown better results in similar studies [1] [2] [3] [4], and thereby motivates for further studies regarding its implementation and applications.

Keywords: Wheel rotation, aerodynamics, drag, MRF, sliding mesh, CFD.

Acknowledgements

Firstly, I would like to express my sincere gratitude to my supervisor, Simon Lindberg, for his constant support and for pushing me always in the right direction during these challenging months. I would also like to thank him for his insightful recommendations and for teaching me the crafts of a CFD Engineer. A great thanks to everyone at CEVT for giving me the opportunity to work in such an encouraging environment and for the constant support throughout the thesis project.

Also, a big thanks to my thesis examiner Dr. Simone Sebben at Chalmers University of Technology for her valuable advice and for all the help provided when needed. Her door was always open for me to ask questions.

I am also grateful for the lifetime friends I gained during my master's degree. For all those amazing times in Gothenburg. Big thanks to my amazing friends back in Mexico for cheering after me and for their incredible support regardless of the distance.

Finally, I am very thankful to my parents and to my sister for their unconditional support and continuous encouragement throughout my years as a student; for inspiring me and giving me the strength to overcome anything; for helping me become the engineer I am today and for pushing me to be a better person. This accomplishment would not have been possible without them. Thanks for all the love.

Andrés Contreras Uriegas, Gothenburg, August 2018

Contents

List of Figures

List of Tables

1

Introduction

This chapter presents a general overview of road-vehicles aerodynamics and its environmental impact. The background section describes briefly the forces acting on a vehicle as it moves through the air and how these forces affect its performance in terms of fuel/energy economy. Additionally, it explains current validation methods such as, wind tunnel tests and Computer Fluid Dynamics (CFD) simulations with an emphasis on wheel rotation, which lays out the foundation for this thesis.

The second section summarizes the environmental impact of road-vehicles; it illustrates the correlation between road transportation and greenhouse emissions. Moreover, it outlines the impact of aerodynamic optimization in terms of fuel economy. Lastly, different test procedures to determine the levels of pollutants and CO_2 emissions are explained concisely.

1.1 Background

Over the past decade, research has pushed forward the automotive industry towards energy efficient transportation (which is closely related to emissions). Many engineering disciplines have taken the challenge of developing energy efficient vehicles, being automotive aerodynamics one of them. Aerodynamics affects significantly the performance of a vehicle in different ways, from straight line stability and crosswind response to dirt deposition and wind noise. Nonetheless, the focus in this study is on the external aerodynamic forces (i.e. drag and lift).

External aerodynamics studies the forces acting on a road vehicle as it moves through the air. Essentially, three force components and three moments contribute to the dynamic behaviour of a vehicle — drag, lift, and side forces account for the acting forces; while roll, yaw, and pitch constitute the corresponding moments. Furthermore, lift is divided into front and rear components at the front and rear axles. For most of the external aerodynamic development, drag and lift are the foundation in the study of road vehicle aerodynamics.

Fundamentally, drag is the force that opposes a vehicle's motion and it can be divided into its pressure and frictional components. In road vehicles, pressure drag is a caused by the pressure distribution around the vehicle; and friction drag is caused by the friction on the surface of the vehicle (shear stress). In a passenger vehicle, the pressure drag is significantly larger compared to friction drag and thus its minimization is the main objective of road vehicle aerodynamics [6]. These components together account for the total drag. Drag is traditionally expressed as a nondimensional coefficient noted as drag coefficient (C_D).

On the other hand, lift contributes significantly to the handling of the vehicle. Usually, lift is associated with airplanes and is defined as the normal component of the force acting on the vehicle's surface due to the pressure difference between the underbody and the roof. Similarly to drag, lift is expressed as a nondimensional coefficient noted as lift coefficient (C_L). Both the C_D and C_L define the aerodynamic performance of a specific vehicle shape.

Throughout the history of automobiles; mechanical design and aesthetics have driven their development. At first, vehicles were designed to accommodate the passengers and isolate them from the weather conditions, neglecting completely the influence of aerodynamics. As cruising speeds increased and the road conditions improved, road vehicle aerodynamics became a significant area of research. [7]

The application of aerodynamic concepts signified a reduction in the drag coefficient and thus a noticeable impact on the energy losses of passenger vehicles. Therefore, road vehicle aerodynamics has been a major contributor to the improvements in energy efficiency. However, aerodynamic optimization represents a major challenge for engineers. Road vehicles are sophisticated shapes moving in close proximity to the ground. In addition, they come in all shapes and sizes, to satisfy many and mixed purposes. The engine compartment, cooling flow, underbody, and rotating wheels add to the complexity of the numerous shapes.

All exterior components, wheels, wheel housings, rear-view mirrors as well as the underbody and engine compartment contribute to the overall drag of the vehicle. The exterior contributes to roughly 50% of the total drag, the wheels and wheel houses account for $25 - 30\%$ and the remaining $20 - 25\%$ is caused by the underbody and engine compartment [8] [9] [10]. It should be noted that these values are approximations and should be considered as such, different vehicle types will have a distinctive drag distribution. Moreover, it is vital to understand that the total drag contribution of a specific zone is not exclusively due to the design of a specific component. For example, modifying a vehicle's front end will have an effect on the pressure distribution between the front and the rear. Hence, aerodynamic validation and optimization takes into account the complete vehicle.

Traditionally, aerodynamic validation is performed in a wind tunnel where the conditions of a vehicle moving straight forward at a constant speed are replicated. In a wind tunnel, the vehicle is fixed with its tyres resting on a moving belt to imitate the wheel rotation. In addition to this, the moving ground is reproduced with a central moving belt. Supplementary boundary control systems are applied to further imitate the real driving conditions. Prior studies [9] [8] [10] have proven the effects of rotating wheels and moving ground in wind tunnel tests. Thus, these two conditions are essential to close down the gap between a real-case scenario and an experimental one. Current wind tunnel technology is able to measure accurately the aerodynamic forces. However, these tests require a significant amount of resources and are often performed late in the design phase. During the past two decades, Computational Fluid Dynamics (CFD) and CPU performance improvements enable engineers to perform more detailed virtual simulations. Thus, further optimize the aerodynamic performance of a vehicle at earlier phases of its design for a fraction of the cost.

Regardless of the fast-paced advancements in the field, CFD simulations are still an approximation of the real case scenario relying on assumptions and mathematical models, ranging from simple models to complex models. These assumptions and different models lead to a difference between the numerical simulations and wind tunnel results. However, the correlation between CFD simulations and experimental results is, in general, accepted by multiple academic publications [11] [12] [13].

As mentioned above, rotating wheels add to the complexity of the flow field, and thus simulating their motion completely in CFD would be costly in terms of computational resources. Hence, their rotation is approximated. The rotation of the wheel is commonly modelled using the Multiple Reference Frame (MRF) approach for the rotation of the rims and a moving/rotating wall (RW) condition for the tyres. In the MRF method, an artificial momentum is added to the flow within a zone defined by the user. This condition aims to replicate the effect that rotating the geometry would have without actually moving the wheels. On the other hand, in the moving wall approach a tangential velocity is specified to wall boundary; for the tyres, this motion is rotational.

Despite using approximated methods to mimic the wheel rotation, previous research [12] [13] proved a good correlation between numerical and wind tunnel results. Nevertheless, latter research [1] [2] [3] [4] demonstrated improved correlation to wind tunnel tests using a sliding mesh (SM) approach and thus presents more opportunities to further study the flow field around the wheels and how it affects the rest of the vehicle. Nowadays, available computer resources and technology enable engineers to simulate in more detail the rotation of the wheels without relying on over simplified CFD procedures.

1.2 Environmental Impact of Vehicle Aerodynamics

In the past century, the global temperature has experienced a notable increase due to mankind. Over its long history, our planet has sustained temperature changes; it has warmed and cooled repeatedly. However, a rapid increase in Earth's average temperature has lead to the melting of the polar ice caps and consequently a rise of the water levels. This phenomenon is commonly known as global warming; and it arises primarily due to a high concentration of greenhouse gases released as a result of burning fossil fuels.

Human-released gases come from many sources; electricity and heat production, agriculture, forestry, and transportation, to mention a few. In Europe, the transport sector represents almost a quarter of the total greenhouse emissions [5].

Figure 1.1 (a) illustrates the greenhouse gases (GHG) emissions due to the transport sector in 2015. From the total emissions, road transport accounts for nearly three quarters. Additionally, figure 1.1 (b) shows the contribution from different road vehicles to the total road transport emissions. Of the total road transport emissions, 44.4% come from passenger cars, while 18.8% from heavy trucks and buses.

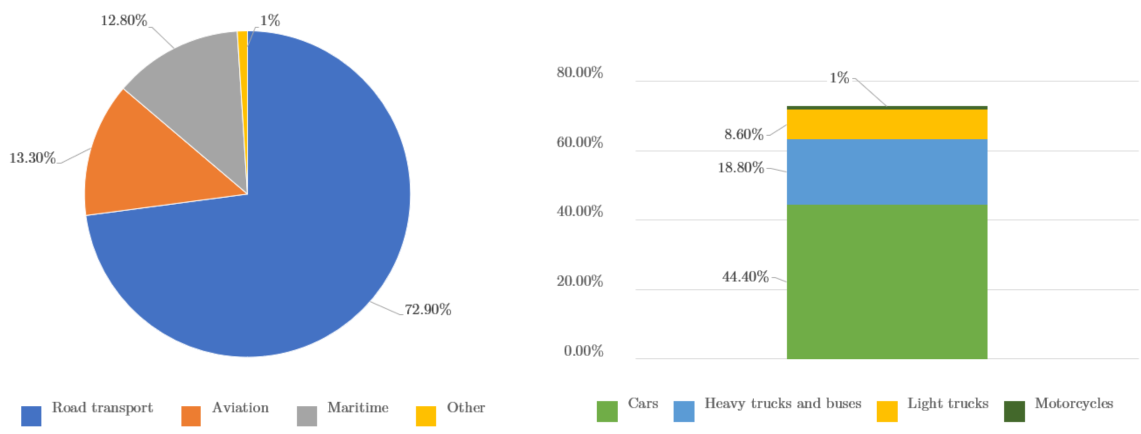

(a) Transport share of GHG emissions.

(b) Road-transport share of transport GHG emissions.

Figure 1.1: Greenhouse emissions (GHG) in Europe 2015 from transport. Source: [5].

In a vehicle, the fuel consumption depends on the efficiency of the powertrain, and the power to overcome the resistance to motion. Without considering the powertrain and internal vehicle forces, the overall driving resistance, F_{Drive}, given in N, is expressed by the sum of the rolling resistance, aerodynamic drag, grade resistance (depending on the inclination of the road) and the acceleration of the vehicle [7]. The total drive force is written as follows in equation (1.1).

$$F_{Drive} \approx F_A + F_D + F_R + F_G \tag{1.1}$$

Where F_A is the acceleration force, F_R is the rolling resistance force, F_G is the gradeability resistance force, and F_D is the aerodynamic resistance force.

If the vehicle is driving on a flat road (inclination angle $\alpha = 0$) at constant speed, equation (1.1) is reduced to the rolling resistance and aerodynamic resistance. Thus, the total force needed to sustain constant motion on a flat road is written as follows in equation (1.2).

$$F_{Drive} \approx \underbrace{F_D}_{\text{Aerodynamic}} + \underbrace{F_R}_{\text{Rolling}}$$

$$F_{Drive} \approx \frac{1}{2}\,\rho\, C_D\, A_F\, v^2 + [(Normal\ Load)\,(C_{RR})] \tag{1.2}$$

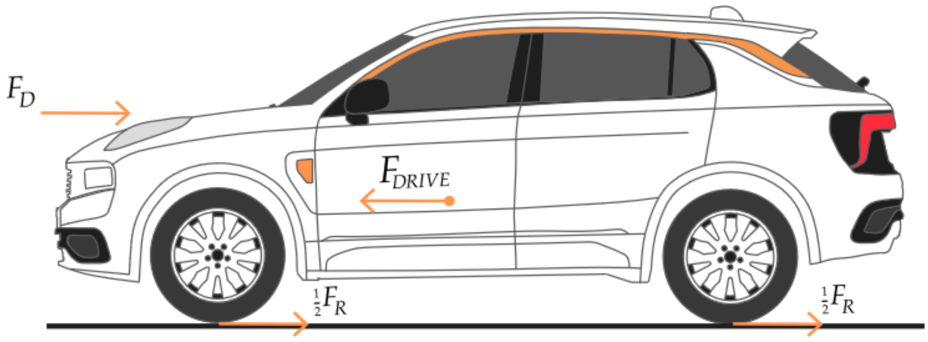

Figure 1.2: Force to overcome motion on a flat road.

The rolling resistance F_R, is produced by different factors; from the rubber mix and tyre temperature to the inflation pressure and tread pattern. In general, the rolling resistance is nearly directly proportional to the normal load applied on the tyres and the rolling resistance coefficient C_{RR} [14]. The rolling resistance is written as follows in equation (1.3)

$$F_R = (\text{Normal Load})\,(C_{RR}) \tag{1.3}$$

The aerodynamic drag F_D, is defined by the air density ρ, the drag coefficient C_D, vehicle's cross sectional frontal area A_F, and the driving speed v. The aerodynamic drag is written as follows in equation (1.4)

$$F_D = \frac{1}{2}\,\rho\, C_D\, A_F\, v^2 \tag{1.4}$$

Both the aerodynamic resistance and the rolling resistance are speed dependent, figure 1.3(a) illustrates both resisting forces as a function of speed. As noted in equation (1.4), the aerodynamic drag F_D increases with the square of the vehicle's speed, while with the other variables only increases marginally. From figure 1.3(a), it is noticeable how as speed builds up the aerodynamic resistance becomes more meaningful than the rolling resistance.

At 100 km/h, the aerodynamic drag accounts for nearly 70% of the total road resistance and thus, most of the effort for improving fuel economy within aerodynamics is by reducing drag. Figure 1.3(b) shows how the aerodynamic force curve shifts due to a 10% and 20% reduction on the C_D value. On the other hand, in the case of hybrid vehicles, drag assumes a grater importance in achieving low fuel consumption and consequently an increase in range [14].

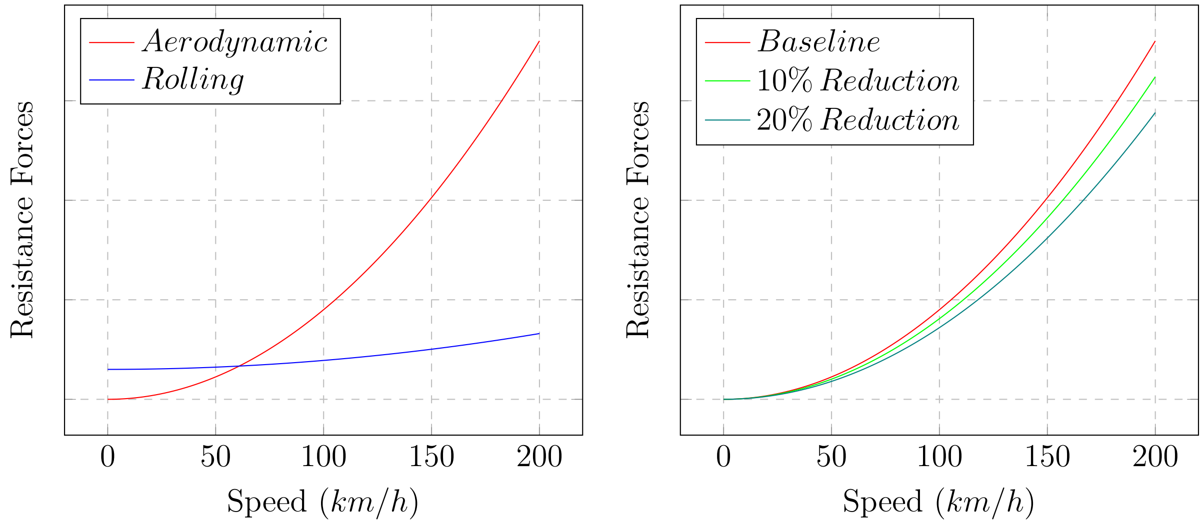

(a) Aerodynamic and tyre rolling resistance vs. cruising speed.

(b) 10% and 20% C_D reduction.

Figure 1.3: Aerodynamic and tyre rolling resistance with respect of cruising speed.

International organizations and governments all around the world have developed stricter policies to ensure a sustainable future. Through initiatives like the Paris Agreement, the shift towards low-emission mobility has started globally and its pace will continue to accelerate after the full implementation (September 2018) of newer emission test procedures like the Worldwide harmonized Light Vehicles Test Procedure (WLTP), which incorporates the Worldwide harmonized Light vehicles Test Cycles (WLTC).

Essentially, WLTC is a new test cycle developed using real-driving data and thus captures better the everyday driving profiles. Compared to its predecessor (NEDC), the WLTC is a dynamic cycle, it has a longer duration, faster acceleration and a higher speed. As part of the new testing cycle, automakers must show the emission values for all possible configurations of a model and not only a base model like it used to be before. This means that any purchasable configuration offered by the manufacturer will be required to show the fuel consumption for that specific model. Table 1.1 outlines the main differences between NEDC and WLTC.

Table 1.1: NEDC vs. WLTC.

	NEDC	**WLTC**
Test Cycle	Single test cycle	Dynamic cycle
Cycle Time	20 min	30 min
Cycle Distance	11 km	23.25 km
Driving Phases	2 phases	4 phases
Urban Phase	66%	52%
Non-urban Phases	34%	48%
Average Speed	34 km/h	46.5 km/h
Maximum Speed	120 km/h	131 km/h

Car manufacturers offer external add-ons like different rims, roof spoilers, exterior styling kits, or load carriers. Therefore, the aerodynamics properties of a vehicle will vary from one configuration to another. For example, the drag and/or lift values of a given vehicle will be different if a different set of wheels is used and thus the fuel consumption will be different as well.

In general, a vehicle has a numerous model variants, and thus running tests to obtain the fuel consumption value for each one of them would be costly. On the other hand, CFD simulations allow engineers to assess any possible concept without the need of performing physical tests.

1.3 Objectives

The aim of this thesis is to investigate sliding mesh as a method for wheel rotation modelling on different rim geometries. Thereafter, the acquired results will be compared to wind tunnel results previously obtained by CEVT. The change in C_D, C_{FL} and C_{RL} from different rims ($\Delta\, C_D$, $\Delta\, C_{FL}$ and $\Delta\, C_{RL}$) will be compared between the sliding mesh approach and the wind tunnel.

Additionally, the flow field is analyzed with the aid of post-processing tools to understand why a given rim produces less or more drag, front-lift and rear-lift.

The Computer Aided Design (CAD) model used for this study is an SUV provided by CEVT. The model includes a detailed underbody and engine compartment. All numerical simulations were performed with ANSYS Fluent 19.0. Figure 1.4 shows an isometric view of the CAD model.

Figure 1.4: SUV CAD model.

1.4 Limitations

The limitations in this study are comparable to the limitations found in any CFD problem. In general, a CFD simulation is limited to a number of factors; CAD geometry simplifications, computational power available and time to mention a few. Many of the limitations listed below are related to a time constraint.

1. This study is limited to a time period of approximately 20-25 weeks. Hence the number of simulations performed needs to fit in this time range.

2. Slick tyres were used in all the cases simulated in this study. Hence, the effects due to the tyre geometrical details are not considered.

3. The ideal CFD-rotation model for wheels would be sliding mesh for both the rim and tyre. However, the tyres are usually deformed at the contact patch due to centrifugal forces and the normal loads applied on it. Thus, making the tyres non axisymmetric and impossible to model as a sliding mesh.

4. The interfaces for the MRF cases are not optimized, and the magnitude for this induced error is not studied in this thesis.

5. The main focus of this study is on the wheel rotation modelling with a special interest on the rims. However, in order to increase the accuracy of the results, the rotation of the brake discs should be considered.

6. The sliding mesh approach was implemented to a small number of cases. Therefore, to generalize the observed trends for a larger number of cases, the study should have performed more simulations under the same conditions.

2

Theory

This chapter provides a theoretical framework upon this thesis is based. First, the physical principles of fluid dynamics are explained in brief. Thereafter, the aerodynamic forces section describe the forces and moments created as a car moves through the air; being drag and lift the fundamental components of this report.

The governing equations and turbulence sections outline the mathematical expressions upon which all of fluid dynamics analysis is based. Lastly, the different methods to simulate the wheels rotation are explained.

2.1 Fluid Dynamics

In engineering, the movement of gas or liquid (collectively called 'fluid') is called 'flow', and the study of fluid flow is known as 'fluid dynamics'. The flow of air and water in our environment have always been flows of our concern, so are the flows in man-made devices. Historically, the need to understand fully the motion of fluids has been hindered by the fact that, in general, the flow of a fluid is irregular.

Fluid matter is made up of discrete molecules, which are always in state of random motion, colliding to each other and with the walls of the container in which they are held. To study matter at a microscopic (molecular) level is relevant for understanding a variety of phenomena. However, studies at these scales are not of interest to solve common engineering problems and thus, fluid matter is studied at a macroscopic level also known as *continuum*.

In *continuum*, it is essential to assume that the discrete nature of matter can be neglected, provided the length scales of interest are large compared with the length scales of discrete molecular structure. Therefore, matter at sufficiently large scales can be treated as *continuum* in which all physical properties such as density, pressure, temperature, and velocity are continuously defined at any infinitesimal point [15].

In road vehicle aerodynamics studies the interaction between the air and the moving vehicle. Nearly all vehicles, run at speeds which are lower than the speed of sound. At a speed below $0.3\,mach$ ($\approx 357km/h$) the variations of pressure and temperature in the flow field vary little from those of the free stream values, and thus the corresponding density changes can be neglected. Hence the fluid can be regarded as incompressible flow [6].

The cornerstone in fluid dynamics are the conservation laws — conservation of mass, conservation of momentum, and conservation of energy. The equations required to characterize the flow are derived from these laws and they are known as the Navier-Stokes equations. The Navier-Stokes equations are essentially applied in all fluid dynamics problems; either in their full or simplified form, these equations are used in the design of aircraft and road vehicles, among many other applications.

For most of the external aerodynamic problems, the forces of interest are the fundamental forces acting on a vehicle: lift, drag, and side force. Being the first two the most significant ones for fuel/energy economy; These forces may be directly measured in an aerodynamic wind tunnel or indirectly with the aid of CFD.

2.2 Aerodynamic Forces

The flow due to a vehicle's motion can be categorized in one of the following groups; the external flow around the vehicle, the internal flow through the vehicle's engine bay, and the flow within the powertrain (engine, exhaust, etc) [6]. In external aerodynamics, the focus is on the forces and moments as a result of the external and internal flows (cooling flow), whereas the flow within the vehicles machinery is regarded separately.

These forces, and moments greatly affect the performance and handling of the vehicle, and are commonly decomposed into three rotational and three translational terms. Figure 2.1 shows the coordinate system used to define the directions of the vehicle dynamic forces and moments.

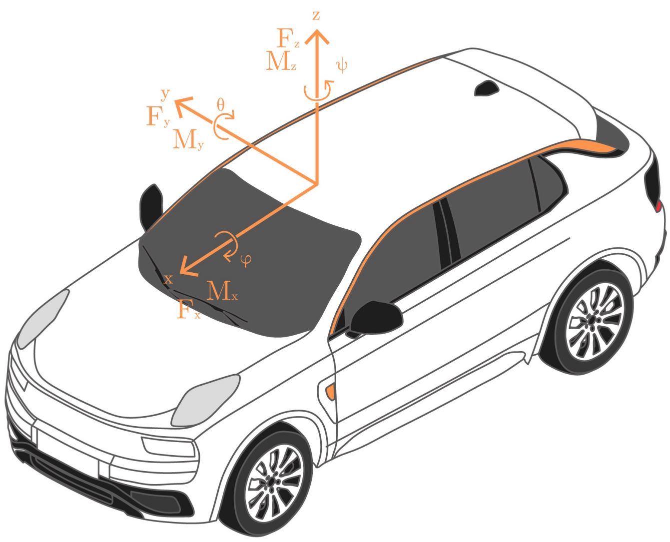

Figure 2.1: Coordinate system, forces and moments on a passenger vehicle.

Three forces and three moments are defined; F_x, F_y, and F_z are the corresponding forces acting on the longitudinal (x), lateral (y) and vertical (z) components. Moreover, M_x (roll), M_y (pitch) and M_z (yaw) are the moments around the previously defined axis system (x, y, z). However, for the purpose of this thesis, the discussion will be limited to the longitudinal and vertical aerodynamic forces.

In essence, two fundamental aerodynamic forces act on a moving vehicle at zero yaw angle. The first one, and the most important in terms of energy consumption, is drag, which is the force that resists the desired motion of the vehicle. It can be divided into pressure drag and friction drag, being pressure drag the dominant source of total drag [6]. The second one is lift, which is the force exerted on the vehicle in the vertical direction (z) due to the pressure difference between the underbody and above the roof. Lift, greatly affects the directional stability of the vehicle.

As noted in section 1.2, the total drag force is written as shown in equation (1.4). Likewise, lift (F_L) is also a function of speed. In addition to the handling effects, lift also influences to a minor extent the fuel economy by affecting the rolling resistance. However, for passenger vehicles this effect is insignificant. In contrast, lift has a significant impact on the motorsport industry where, depending on the race track, a gain in negative lift, also known as downforce, represents a reduction in lap times.

The mathematical expression for the lift force is written as follows in equation (2.1). Where the A_F is a frontal projected area of the vehicle.

$$F_L = \frac{1}{2}\,\rho\, C_L\, A_F\, v^2 \tag{2.1}$$

2.3 Aerodynamic Coefficients

The aerodynamic coefficients are nondimensional numbers which determine the aerodynamic characteristics of a given geometry. As mentioned in section 2.2, there are two fundamental aerodynamic forces acting on the vehicle; drag and lift.

The central idea of nondimensional lift and drag coefficients is to have a value only related to the vehicle's shape, this allows the aerodynamic performance between different vehicles and different setups of the same vehicle to be compared directly.

The drag coefficient is the ratio of aerodynamic force (F_D) to the square of speed (v^2) and the frontal area (A_F). The expression for the drag coefficient is written as follows in equation (2.2).

$$C_D = \frac{2F_D}{\rho v^2 A_F} \tag{2.2}$$

The lift coefficient is obtained in the same way as the drag coefficient. The expression for the lift coefficient is written as follows in equation (2.3).

$$C_L = \frac{2F_L}{\rho v^2 A_F} \tag{2.3}$$

2.4 Governing Equations

The core of fluid dynamics are the fluid governing equations. These equations are derived from the conservation laws — conservation of mass (continuity equation), linear momentum (Newton's second law of motion), and energy (first law of thermodynamics). The above mentioned equations constitute the basic principles upon which fluid dynamics is based.

The mass conservation principle states that the rate of increase of mass in a given system is equal to the net rate of mass flow into the system. Equation (2.4) is an unsteady, three-dimensional mass conservation equation at a point in a compressible fluid.

$$\frac{\partial \rho}{\partial t} + \frac{\partial \rho u_i}{\partial x_i} = 0 \tag{2.4}$$

In the formulation above, the first term on the left side is the rate of change in time (t) of the density (ρ). The second term describes the net flow of mass out of the system across its boundaries and is called the convective term [16].

The momentum conservation law states that the rate of change of momentum of a fluid equals the sum of the forces acting on the fluid. The conservation of momentum equation is written as follows in equation (2.5).

$$\frac{\partial \rho u_i}{\partial t} + \frac{\partial \rho u_i u_j}{\partial x_j} = -\frac{\partial p}{\partial x_i} + \frac{\partial \tau_{ij}}{\partial x_j} + \rho f_i \tag{2.5}$$

Where the last term (ρf_i), is the contribution due to body forces such as the force due to gravity. The viscous stress tensor (τ_{ij}) is defined as written in equation (2.6) in which the strain tensor (S_{ij}) is written as follows in equation (2.7)

$$\tau_{ij} = 2\mu S_{ij} - \frac{2}{3}\mu S_{kk}\delta_{ij} \tag{2.6}$$

$$S_{ij} = \frac{1}{2}(\frac{\partial u_i}{\partial x_j} + \frac{\partial u_j}{\partial x_i}) \tag{2.7}$$

The conservation of energy equation is derived from the first law of thermodynamics, which states that the rate of change of energy of a fluid is equal to the rate of heat addition to the fluid plus the rate of work done.

The continuity energy equations in differential form can be written as follows in equations (2.8).

$$\frac{\partial \rho E}{\partial t} + \frac{\partial \rho u_j E}{\partial x_j} = -\rho q + \frac{\partial}{\partial x_j}(k\frac{\partial T}{\partial x_j}) - \frac{\partial u_i p}{\partial x_j} + \frac{\partial u_i \tau_{ij}}{\partial x_j} + \rho f_i u_i \tag{2.8}$$

Where E is the total energy of a moving fluid per unit mass, and its defined as $E = e + \frac{1}{2}(V^2)$, where e is the internal energy per unit mass and $\frac{V^2}{2}$ is the kinetic energy per unit mass and the pressure (p) is given by the ideal gas law $p = \rho RT$.

For all flows, the conservation equations for mass and momentum are solved. If the problem involves heat transfer or the flow is compressible, the conservation of energy equation needs to be solved as well.

The scope of this thesis does not involve any heat transfer, thus the flow is assumed to be isothermal. Therefore, only the continuity and conservation of momentum equations are included in this report. Additionally, as mentioned previously, the vehicle speed is significantly smaller than the speed of sound (below $0.3\,mach$), thus the flow is assumed to be incompressible ($\rho = constant$). Equations (2.4) and (2.5) are reduced to the expressions written as follows in equations (2.9) and (2.10) respectively.

$$\frac{\partial u_i}{\partial x_i} = 0 \tag{2.9}$$

$$\rho \frac{\partial u_i u_j}{\partial x_j} = -\frac{\partial p}{\partial x_i} + \frac{\partial \tau_{ij}}{\partial x_j} + \rho f_i \tag{2.10}$$

2.5 Turbulence

Nearly all fluid flow is turbulent. From the flow around road vehicles and airplanes to the flow from combustion in engines and turbines. Thus when computing the flow, it will most likely be turbulent.

In road vehicle aerodynamics turbulent flow is always present. The flow in a turbulent region is chaotic and irregular. It may seem random, but it is governed by the Navier-Stokes equations (see section 2.4). In other words, turbulence is defined by abrupt changes in flow velocity or swirling irregular motion of different scales (eddy sizes).

Despite the complexity and diversity of fluid flows, the Navier-Stokes equations describe them accurately and in complete detail. However, in terms of turbulent flows, Navier-Stokes' detailed description is their advantage and disadvantage at the same time. The equations describe every detail of the turbulent velocity field, from the largest to the smallest length scales. Thus, the amount of information contained in the velocity field is very extensive, and as a consequence the direct approach of solving the Navier-Stokes equations, also known as Direct Numerical Simulation (DNS) is, in general, unpractical. [17].

To solve the Navier-Stokes equations numerically it would require a very fine grid to resolve all turbulent scales and it would also require a fine resolution in time. Hence, DNS is costly in computational resources and time. Instead, a statistical model where the turbulent flow is described in terms mean velocity field is used to represent the turbulent flows. The most common models are: turbulent viscosity models, e.g., the $k - \varepsilon$ or $k - \omega$

models; and large-eddy-simulations (LES) [17].

2.5.1 Reynolds-Averaged Navier-Stokes

As mentioned in the previous section, simplifications of the turbulence flow are done to reduce the computational requirements. The basic element of the Reynolds-Averaged Navier-Stokes (RANS) equations is the Reynolds decomposition, where the instantaneous variables are decomposed into a mean value and a fluctuating value, i.e.

$$u_i = \overline{u_i} + u_i' \tag{2.11}$$

$$p = \overline{p} + p \tag{2.12}$$

Where the overbar denotes the time-averaged value defined as:

$$\overline{u} = \frac{1}{\Delta t}\int_0^{\Delta t} u(t)\, dt \tag{2.13}$$

In theory, the time interval Δt is larger than the time scale associated with the slowest variations (due to the largest eddies). In time-dependent flows the mean of a property at time t is taken to be the average of the instantaneous values of the property over a large number of repetitions. The time average of the fluctuations u' is, by definition, zero:

$$\overline{u'} = \frac{1}{\Delta t}\int_0^{\Delta t} u'(t)\, dt = 0 \tag{2.14}$$

Applying the Reynolds averaging (eq. (2.11) and (2.12)) to the continuity and Navier-Stokes equations, (2.9) and (2.10) respectively, gives as a result the time averaged continuity and Navier-Stokes equation,

$$\frac{\partial \overline{u_i}}{\partial x_i} = 0 \tag{2.15}$$

$$\rho\frac{\partial \overline{u_i}\,\overline{u_j}}{\partial x_j} = -\frac{\partial \overline{p}}{\partial} + \frac{\partial}{\partial x_j}\Big(\mu\frac{\partial \overline{u_i}}{\partial x_j} - \rho\overline{u_i' u_j'}\Big) \tag{2.16}$$

In the formulations above, the term $\rho\overline{u_i' u_j'}$ on the right side of equation (2.16) is known as the Reynolds stress tensor.

2.5.2 RANS-based Models

For most of the engineering problems it is unnecessary to resolve in detail the turbulent fluctuations. In general, the information from the time-averaged properties of the flow is enough for most purposes. Thus, the majority of turbulent flow computations relays on the RANS equations. In order to compute turbulent flows with the RANS equations it is necessary to develop turbulence models to predict the Reynolds stresses. The RANS turbulence models are divided with respect of the number of additional transport equations that need to be solved along with the RANS equations [16].

2.5.3 $k - \omega$ Turbulence Model

The $k - \omega$ is one of the most popular turbulence models used in CFD simulations. It is a two-equation model that solves the RANS equations (2.15) and (2.16) along with two partial differential equations for two variables, in which k accounts for the kinetic energy and ω for the specific rate of dissipation. The transport equations to represent the turbulent properties of the flow are written as follows in (2.17) and (2.18) for k and ω respectively. The eddy viscosity is computed from $\mu_t = \rho k/\omega$.

$$\frac{\partial \rho k}{\partial t} + \frac{\partial(\rho u_j k)}{\partial x_j} = \frac{\partial}{\partial x_j}\left(\left(\mu + \sigma_k \frac{\rho k}{\omega}\right)\frac{\partial k}{\partial x_j}\right) + P - \beta^* \rho \omega k \tag{2.17}$$

$$\frac{\partial \rho \omega}{\partial t} + \frac{\partial(\rho u_j \omega)}{\partial x_j} = \frac{\partial}{\partial x_j}\left(\left(\mu + \sigma_\omega \frac{\rho k}{\omega}\right)\frac{\partial \omega}{\partial x_j}\right) + \frac{\gamma \omega}{k} P - \beta \rho \omega^2 \tag{2.18}$$

Where,

$$P = \tau_{ij} \frac{\partial u_i}{\partial x_j} \tag{2.19}$$

$$\tau_{ij} = \mu_t \left(2S_{ij} - \frac{2}{3}\frac{\partial u_k}{\partial x_k}\right) - \frac{2}{3}\rho k \delta_{ij} \tag{2.20}$$

$$S_{ij} = \frac{1}{2}\left(\frac{\partial u_i}{\partial x_j} + \frac{\partial u_j}{\partial x_i}\right) \tag{2.21}$$

In equations (2.17) and (2.18), the first term from left to right is the rate of change of k or ω; the second term is the transport of k or ω by convection; the third term is the transport of k or ω by turbulent diffusion; the fourth term is the rate of production of k or ω; and the last term is the rate of dissipation of k or ω [16].

2.5.4 GEKO Model

The GEKO (generalized $k-\omega$) model is a two-equation turbulence model based on the $k-\omega$ model. Traditional two-equation turbulence models ($k-\omega$ and $k-\varepsilon$) solve two partial differential equations to obtain two independent scales. Baseline models ($k-\varepsilon$ and $k-\omega$) offer five coefficients ($C_{\omega 1}$, $C_{\omega 2}$, C_μ, σ_k, σ_ω) that can be changed by the user according to the given problem. However, these coefficients are linked to each other and must fulfill a set of conditions. Thus, the traditional $k-\omega$ or $k-\varepsilon$ models do not provide much flexibility, which often results in having different models for different applications.

In contrast, the GEKO model has more flexibility allowing the CFD user to adjust free parameters for specific types of applications, without the negative impact on the basic calibration of the model [18].

The GEKO model is based on a $k-\omega$ formulation and features four coefficients that can be tuned/optimized within given limits. The functions F_1, F_2, and F_3 contain four free coefficients [19];

$$\frac{\partial(\rho k)}{\partial t} + \frac{(\rho u_j k)}{\partial x_j} = P_k - \rho C_\mu k\omega + \frac{\partial}{\partial x_j}\left[\left(\mu + \frac{\mu_t}{\sigma_k}\right)\frac{\partial k}{\partial x_j}\right] \tag{2.22}$$

$$\frac{\partial(\rho\omega)}{\partial t} + \frac{\partial \rho u_j \omega}{\partial x_j} = C_{\omega 1} F_1 \frac{\omega}{k} P_k - C_{\omega 2} F_2 \rho\omega^2 + F_3 \frac{2}{\sigma_\omega}\frac{\rho}{\omega}\frac{\partial k}{\partial x_j}\frac{\partial \omega}{\partial x_j} + \frac{\partial}{\partial x_j}\left[\left(\mu + \frac{\mu_t}{\sigma_\omega}\right)\frac{\partial \omega}{\partial x_j}\right] \tag{2.23}$$

1. C_{SEP} — Changes separation behavior.
   - $1 < C_{SEP} < 2.5$ (default $C_{SEP} = 1.75$)
   - Increasing C_{SEP} leads to earlier and stronger separation.
   - $C_{SEP} = 1$ mimics the standard $k-\varepsilon$ model, $C_{SEP} = 1.75$ is close in performance to the SST mode.
2. C_{MIX} — Changes spreading rates of free shear flows.
   - $0 < C_{MIX} < 1$ (default - correlation $C_{MIX_{COR}} = 0.35\sqrt{(\mid C_{SEP} - 1 \mid)}$)
   - Increasing C_{MIX} leads to stronger mixing in free shear flows (mixing layers). The correlation $C_{MIX_{COR}}$ assures that, for changes in C_{SEP}
3. C_{NW} — Changes near-wall behavior.
   - $-2 < C_{NW} < 2$ (default $C_{NW} = 0.5$)
   - Increasing C_{NW} leads to higher heat transfer rates at reattachment locations.
   - C_{NW} is mostly used to adjust for flows with heat transfer in impingement zones.

It has a very strong default value and typically should not be changed except if detailed experimental data are available.

4. C_{JET} — Optimizes free jet flows.

   · $0 < C_{JET} < 1$ (default $C_{JET} = 0.9$)

   · Increasing C_{MIX} will also increase the spreading rates of free jet flows. This can be undesirable, and therefore C_{JET} allows to reduce the effect of C_{MIX} on free jet flows. C_{JET} is only to active when C_{MIX} is non-zero and reduces the spreading rates of free jets.

2.5.5 LES-based Models

Large Eddy Simulations or LES, is an intermediate form of RANS and DNS where large eddies are resolved directly, while small eddies are modeled. The method involves space filtering of the unsteady Navier-Stokes equations prior to the computations, which passes the larger eddies and rejects the smaller eddies. The effects on the resolved flow (mean flow plus large eddies) due to the small, unresolved eddies, are included by means of a so-called sub-grid scale model.

The filter function $G(x,\, x',\, \Delta)$ is written as follows[16]:

$$\overline{\phi} \equiv \int_{\infty}^{-\infty} \int_{\infty}^{-\infty} \int_{\infty}^{-\infty} G(x,\, x',\, \Delta)\phi(x',\, t)\, dx'_1\, dx'_2\, dx'_3 \tag{2.24}$$

Where,

$$\overline{\phi} = \text{filtered function} \tag{2.25}$$

$$\phi(x,\, t) = \text{original (unfiltered) function} \tag{2.26}$$

$$\Delta = \text{filter cutoff width} \tag{2.27}$$

In the above equations, (2.24) and (2.25), the overbar indicates spatial filtering, not time-averaging like in section 2.5.1.

Filtering the Navier-Stokes equations yields the LES continuity and momentum equations (in differential form) [16]; in the formulations below, the bold overbar, $\bar{\mathbf{u}}$, denotes a filtered flow variable.

$$\frac{\partial \rho}{\partial t} + \mathrm{div}(\rho \bar{\mathbf{u}}) = 0 \tag{2.28}$$

$$\frac{\partial(\rho\overline{u})}{\partial t} + \mathrm{div}(\rho\overline{u}\bar{\mathbf{u}}) = -\frac{\partial \overline{p}}{\partial x} + \mu\,\mathrm{div}(\mathrm{grad}(\overline{u})) - (\mathrm{div}(\rho\overline{u\mathbf{u}}) - \mathrm{div}(\rho\overline{u}\bar{\mathbf{u}})) \tag{2.29}$$

$$\frac{\partial(\rho\overline{v})}{\partial t} + \mathrm{div}(\rho\overline{v}\bar{\mathbf{u}}) = -\frac{\partial \overline{p}}{\partial y} + \mu\,\mathrm{div}(\mathrm{grad}(\overline{v})) - (\mathrm{div}(\rho\overline{v\mathbf{u}}) - \mathrm{div}(\rho\overline{v}\bar{\mathbf{u}})) \tag{2.30}$$

$$\frac{\partial(\rho\overline{w})}{\partial t} + \mathrm{div}(\rho\overline{w}\bar{\mathbf{u}}) = -\frac{\partial \overline{p}}{\partial z} + \mu\,\mathrm{div}(\mathrm{grad}(\overline{w})) - (\mathrm{div}(\rho\overline{w\mathbf{u}}) - \mathrm{div}(\rho\overline{w}\bar{\mathbf{u}})) \tag{2.31}$$

Solving only the large eddies allows the CFD user to use a much coarser mesh and large time-step sizes in LES than in DNS. However, LES still requires substantially finer meshes than those typically used for RANS calculations. Additionally, LES has to be run for a sufficiently long flow-time to obtain stable statistics of the flow being modeled. As a result, the computational cost involved with LES is normally orders of magnitude higher than that for steady RANS calculations in terms of memory (RAM) and CPU time.

The unsteady-state numerical simulations described in this report are solved using a hybrid RANS-LES model called Stress Blended Eddy Simulations (SBES). A brief summary of the turbulence model is presented in the following subsection.

2.5.6 Stress-Blended Eddy Simulations (SBES)

Stress-Blended Eddy Simulations (SBES) is a hybrid RANS-LES turbulence model. Fundamentally, SBES allows different RANS and LES models to be combined, using a so-called blending function to switch between them automatically.

SBES is a model derived from DDES (Delayed Detached Eddy Simulations). In DDES, the primary goal is to model the attached and mildly separated boundary layers in RANS mode and then switch to LES mode for separated (detached) shear layers. Starting from a given RANS model, a DDES formulation is achieved in two-equation models by a modification of the sink term in the $k-$equation. In the $k-$equation of the SST model, the modification is reformulated as follows:

$$\varepsilon_{DDES} = -\beta^* \rho k \omega F_{DDES} \tag{2.32}$$

Where,

$$F_{DDES} = \Big(\max\Big(\frac{L_t}{C_{DES}\Delta_{max}}\Big(1 - f_{DDES}\Big), 1\Big) - 1\Big) \tag{2.33}$$

Furthermore, the shielding function, f_{SDES}, can be extended to achieve a blending on the stress level between RANS and LES formulations. In general terms, this affects the turbulence stress tensor in the following way:

$$\tau_{ij}^{SBES} = f_{SDES}\tau_{ij}^{RANS} + (1 - f_{SDES})\tau_{ij}^{LES} \tag{2.34}$$

Where τ_{ij}^{RANS} is the RANS portion and τ_{ij}^{LES} is the LES portion of the modeled stress tensor. In cases where both models are based on eddy viscosity concepts, the formulation simplifies to:

$$\nu_t^{SBES} = f_{SDES}\nu_t^{RANS} + (1 - f_{SDES})\nu_t^{LES} \tag{2.35}$$

The main advantage of the SBES model is that it allows the CFD user to use a given LES model in the LES portion of the flow, instead of relying on the LES capability of DES-like models.

2.6 Computational Fluid Dynamics (CFD)

The formulations described in the previous sections are the foundation of CFD, which is a tool used to compute fluid dynamic problems virtually. In CFD the flow of a fluid is analyzed based on its physical properties such as velocity, pressure, temperature, density, and viscosity. To virtually generate a solution the problem is divided into different stages. First, the user constructs a computer model (CAD model) of the physical case, this is known as the computational domain. Second, the computational domain is divided into a finite number of elements. Thereafter, the equations described in section 2.4 are used to construct a mathematical model that describes changes on those physical properties for both the fluid flow and the model geometry. Finally, a number of boundary conditions and physics (like pressure, temperature, density, velocity of the flow at the inlet, etc) are defined by the user and the problem is resolved by means of computer-based simulations.

The following subsections highlight the different wheel rotation modeling methods used in the CFD simulations for this report. Additional information regarding CFD simulations can be found in [16]. In addition, the Methodology chapter (see section 3) covers the CFD-setup for all the cases carried out in the thesis.

2.7 Wheel Rotation Modelling

The angular velocity of the wheels can be modelled in various ways. Traditionally, a MRF boundary condition is applied on a region containing the rim spokes and a RW condition on the tyre. This method is a standard practice in the automotive industry. However, less popular methods, like sliding mesh are also utilized. The different methods to model wheel rotation are described in the following subsections.

2.7.1 Rotating Wall

The Rotating Wall (RW) method is, possibly, the simplest way of modelling wheel rotation. In this approach, the rotational option allows the user to specify a rotational velocity about a specified axis. The velocity is applied tangentially to each cell of the specified boundary; Then, the CFD solver determines the individual cell velocity based on the distance to to the axis of rotation and the angular speed. The tangential rotational motion will be correct only if the wall bounds a surface of revolution about the prescribed axis of rotation (e.g., a circle or cylinder).

To define the rotation axis, the rotation-axis direction and rotation-axis origin is required. For 3D problems, the axis of rotation is the vector passing through the specified rotation-axis origin and parallel to the vector from $(0,0,0)$ to the (x,y,z) point specified under rotation-axis direction.

2.7.2 Multiple Reference Frame

The Multiple Reference Frame (MRF) method is a steady-state approximation in which the CFD user determines a number of cell zones (or MRF regions) with defined interfaces between the zones. In each individual cell zone, the user can define different rotational speeds. Thereafter, the flow in each moving cell zone is solved using the moving reference frame equations. For the absolute velocity formulation, the governing equations of fluid flow for a steadily moving frame can be written as follows in equations (2.36), (2.37) and (2.38).

$$\frac{\partial \rho}{\partial t} + \nabla \cdot \rho \overrightarrow{v_r} = 0 \tag{2.36}$$

$$\frac{\partial}{\partial t}\rho \overrightarrow{v} + \nabla \cdot (\rho \overrightarrow{v_r}\,\overrightarrow{v}) + \rho[\overrightarrow{\omega} \times (\overrightarrow{v} - \overrightarrow{v_t})] = \nabla p + \nabla \cdot \overline{\overline{\tau}} + \overrightarrow{F} \tag{2.37}$$

$$\frac{\partial}{\partial t}\rho E + \nabla \cdot (\rho \overrightarrow{v_r} H + p \overrightarrow{u_r}) = \nabla \cdot (k \nabla T + \overline{\overline{\tau}} \cdot \overrightarrow{v}) + S_h \tag{2.38}$$

The notation used in the above mentioned equations is taken from Fluent's Theory Guide [19].

In this formulation, the Coriolis and centripetal accelerations can be simplified into a single term ($\overrightarrow{\omega} \times (\overrightarrow{v} - \overrightarrow{v_r})$). In the above equations, $\overrightarrow{v_r}$ is the relative velocity with respect to the moving frame, $\overrightarrow{v}$ is the absolute velocity, $\overrightarrow{u_r}$ is the velocity of the moving frame relative to the inertial reference frame, $\overrightarrow{v_t}$ is the translational frame velocity, and $\overrightarrow{\omega}$ is the angular velocity, $\overrightarrow{F}$ are the body forces p is the fluid pressure, and ρ is the fluid density.

If the zone is stationary ($\omega = 0$), the equations reduce to their stationary form. At the interfaces between cell zones, a local reference frame transformation is performed to enable flow variables in one zone to be used to calculate fluxes at the boundary of the adjacent zone.

It should be noted that the MRF approach does not account for the relative motion of a moving zone with respect to adjacent zones (which may be moving or stationary); the mesh remains fixed for the computation. This is analogous to freezing the motion of the moving part in a specific position and observing the instantaneous flow field with the wheel in that position.

While the MRF approach is clearly an approximation, it can provide reasonable model of the flow for many applications. For example, the MRF model is dominantly used in the automotive industry to model the radiator's cooling fan.

However, the MRF approach has a number of limitations. The interfaces defined by the user affects the outcome. Additionally, for a geometry that is not axisymmetric, the positioning of the model during the simulation can also have a significant impact on the ultimate results. For example, the results from two CFD simulations where the only difference is the position of the spokes will differ from each other due to the orientation of the rims.

2.7.3 Sliding Mesh

The sliding mesh model is particular case of general dynamic mesh motion wherein the nodes move rigidly in a given dynamic cell zone(s). In other words, the nodes contained within a defined a cell zone(s) will move each time step with respect the neighboring cell zones. Thus, an interface between the sliding mesh region and the rest of the domain is needed. This interface, needs to be updated every time step as well.

The generic transport equation for dynamic meshes (2.39), is written as follows in equation (2.39).

$$\frac{d}{dt}\int_V \rho\phi dV + \int_{\partial V} \rho\phi(\overrightarrow{u} - \overrightarrow{u_g}) \cdot d\overrightarrow{A} = \int_{\partial V} \Gamma\nabla\phi \cdot d\overrightarrow{A} + \int_V S_\phi dV \tag{2.39}$$

Where,

ρ is the fluid density

$\overrightarrow{u}$ is the flow velocity vector

$\overrightarrow{u_g}$ is the mesh velocity of the moving mesh

Γ is the diffusion coefficient

S_ϕ is the source term of ϕ

∂V is used to represent the boudary of the control volume V

It should be noted that the generic transport equation for dynamic meshes, equation

(2.39) also applies for sliding meshes.

By using a first-order backward difference formula, the time derivative term in equation (2.39) can be written as:

$$\frac{d}{dt}\int_V \rho\phi dV = \frac{(\rho\phi V)^{n+1} - (\rho\phi V)^n}{\Delta t} \tag{2.40}$$

Where, n and $n+1$ indicate the quantity at the current and next time level respectively. The $(n+1)$th time level volume, V^{n+1}, is computed from:

$$V^{n+1} = V^n + \frac{dV}{dt}\Delta t \tag{2.41}$$

Because the mesh motion in the sliding mesh formulation is rigid, all cells retain their original shape and volume. Thus, the time rate of change of the cell volume is zero.

$$V^{n+1} = V^n \tag{2.42}$$

Thus, equation (2.40) simplifies to:

$$\frac{d}{dt}\int_V \rho\phi dV = \frac{[(\rho\phi)^{n+1} - (\rho\phi)^n]V}{\Delta t} \tag{2.43}$$

Equation (2.39) together with the above simplifications, permits the flow in the sliding mesh cell zone(s) to be updated, provided that an appropriate specification of the rigid mesh motion is defined for each zone. Given that the mesh is moving, the solutions to equation (2.39) for sliding mesh applications will be inherently unsteady (as they are for all dynamic meshes) [19].

3
Methodology

In this chapter, the set up for the different cases is explained. First, the geometry for the computational domain of interest is pre-processed and an initial surface mesh is generated. Thereafter, the surface wrapping and volume mesh is created in ANSYS Fluent Mesh 19.0; where a number of refinements are applied accordingly. In addition, the mesh is refined even further in ANSYS Fluent Solver 19.0 to obtain the final mesh; also in Fluent Solver, a number of boundary conditions are defined including the wheel rotation modelling and turbulence model.

The simulation is resolved in two steps. First, the MRF/RW method is implemented and the case is solved in steady-state using GEKO as the turbulence model. Following, the sliding mesh method is implemented and the simulation is solved in unsteady with SBES as the turbulence model. It is worth mentioning that for the second part, the steady-state solution is used as starting point.

3.1 Model Preparation

An existing CAD model of a production SUV with complete underbody and open engine compartment was provided by CEVT. Additionally, two CAD models of different rims were given. The model clean up and preparation was done in ANSA v.17, a CAE pre-processing tool. The changes were primarily regarding the rims and part naming (known as PIDs in ANSA v.17). For all the cases, the rims had to be aligned with the corresponding rotation axle and properly assembled. Moreover, the interface surfaces were created for each set of rims independently.

The complete vehicle and the different rims are shown in figures 3.1 and 3.2 respectively. It is important to remark that the tyres used are slicks for all the cases. Thus, no rain grooves, edge pattern, side grooves, dimples or any other details. Previous academic publications have shown the influence of tyre profile and tyre pattern on drag and lift values [3] [20]. However, to keep simulations less computationally expensive, it was decided to use slick tyres.

For (c) and (d) in figure 3.2, the 18" *A* rim is used as a baseline. In (c), only half of the openings are covered with surfaces. In (d) the complete outer face of the rim is covered. It should be noted that the inside of the rim is like the original 18" *A* rim (a). This is done in order to replicate the geometry set-up from the wind tunnel tests. It is worth

(a) Front view.

(b) Isometric view.

Figure 3.1: Vehicle geometry used in all simulations.

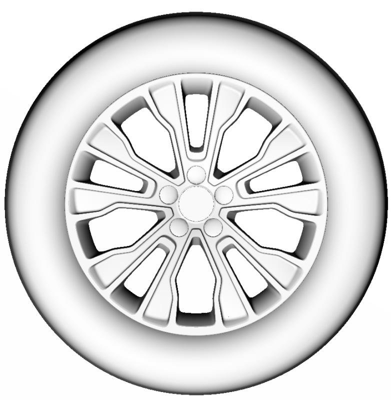

(a) 18" *A* rim.

(b) 19" *B* rim.

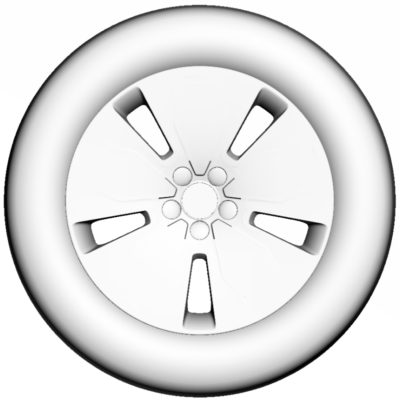

(c) 18" half-covered *A* rim.

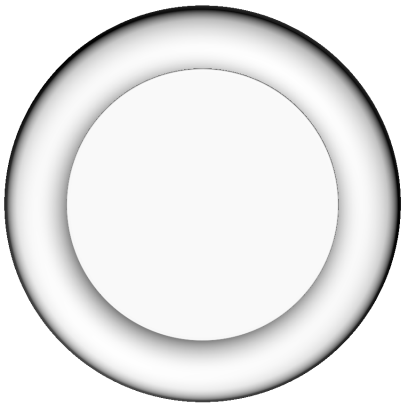

(d) 18" full-covered *A* rim.

Figure 3.2: Different rim geometries used.

mentioning that all numerical simulations were carried out on a full vehicle due to the asymmetric underbody and engine compartment. Moreover, the full name of the rims is not used and thereby they are regarded as "A, B, half-covered A and fully-covered A" according to the order they appear in figure 3.2.

3.1.1 Sliding Mesh Region

In order to implement a sliding mesh condition, a region needs to be specified and thus an interface is needed. For the cases described in this study, two different sets of interfaces were created with a variation on one of them thus three different sets of interfaces in total. The inner and outer interfaces (marked in red) are shown in figure 3.3 (a) and (b) respectively.

The region contained within the interfaces includes only the non axisymmetric parts of the rim. Hence, only the spokes and neighbouring regions are contained. The interfaces were created with two objectives in mind. One, to avoid bad cells while generating the mesh between the brake calipers and the interface, and the second is to minimize the number of faces to reduce meshing complexity.

In addition to the above mentioned reasons, it was found that faces which angle was $\approx 140°$ were prone to bad cells near their common edge. Thus, producing errors in the unsteady part of the simulations.

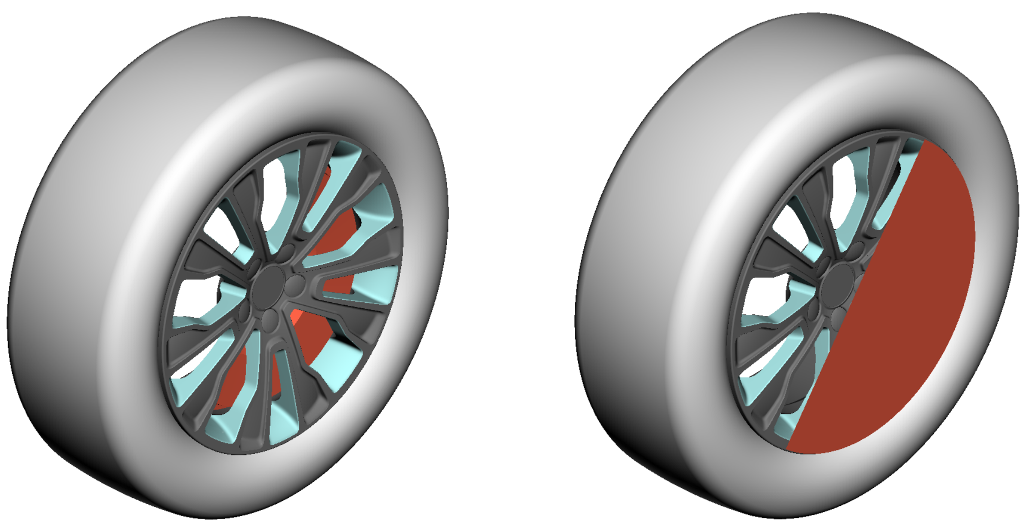

(a) Inner interface for 18" A rims. **(b)** Outer interface for 18" A rim.

Figure 3.3: Interface used for SM and MRF.

The interfaces between the fluid domain and the sliding mesh cell zone are critical. Special attention was paid when meshing the interfaces. Furthermore, each set of rims requires a specific set of inner and outer interfaces. For example, if the rim is bigger, the space between the brake calipers and the inner wall of the rims is larger and thus the interface will be larger as well. As an example, the interfaces used for the 18" A rim case are shown under figure 3.4, where (a) and (c) are illustrates the rim alone and (b) and (d) illustrate the interfaces.

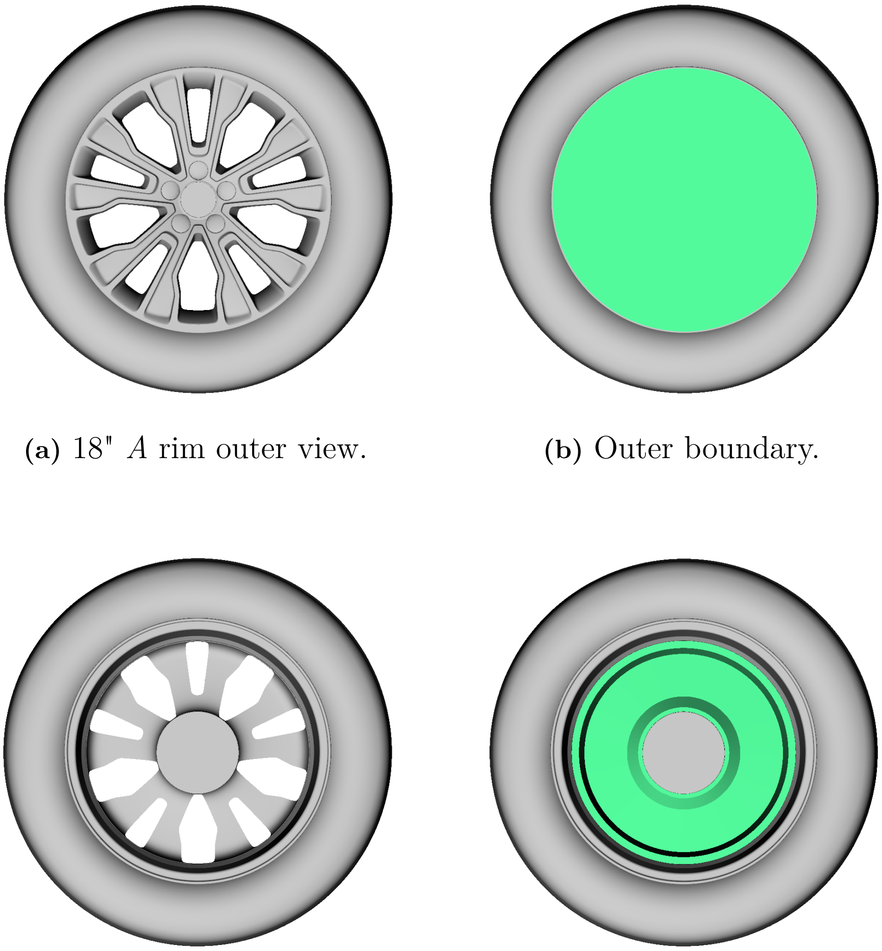

(a) 18" *A* rim outer view.

(b) Outer boundary.

(c) 18" *A* rim inner view.

(d) Inner boundary.

Figure 3.4: SM and MRF Boundaries

Section 2.7.2 briefly mentions the drawbacks of MRF. Being the induced pressure gradient one of the main flaws when using MRF. However, for simplicity in this study, the interfaces created for sliding mesh will be used also for MRF. The induced pressure gradient is assumed to be similar in all cases and thus the cases are considered as part of the results.

3.2 Surface Mesh

As mentioned in the previous sections in this chapter. ANSA v.17 was used to pre-process the geometry. After defining the interfaces and setting correctly the PID's; an initial surface mesh is generated; where parts of the model like the engine, transmission, suspension, electric wiring and brakes were wrapped previously. This surface mesh is then imported to ANSYS Fluent Mesh 19.0.

In Fluent Mesh 19.0, the mesh input from ANSA is re-meshed and wrapped again; following, the vehicle parts are grouped into specific objects (e.g. exterior, suspension, underbody, cooling pack, etc.). Thereafter, the six faces of the virtual wind tunnel are generated followed by the creation of six different bodies of influence (BOIs) for the body and two for the wheels, to which different mesh refinements are applied during the volume meshing.

3.3 Volume Mesh

To simulate the air flow around the vehicle, a volume mesh is needed, which essentially is a grid of the space enclosed by the virtual wind tunnel. The virtual wind tunnel is a rectangular volume that consists of a inlet, outlet, two sidewalls, roof and ground surface. The size of the volume is $80\,m \times 20\,m \times 15.11\,m$ (length × width × height). Everything within the tunnel is referred as the computational domain. Figure 3.5 shows a schematic diagram of the vehicle within the tunnel.

The vehicle is located laterally centered within the virtual tunnel with its front end placed at about one quarter of the tunnel length. For simplicity, the contact patch is replicated by intersecting the ground plane with the tyres.

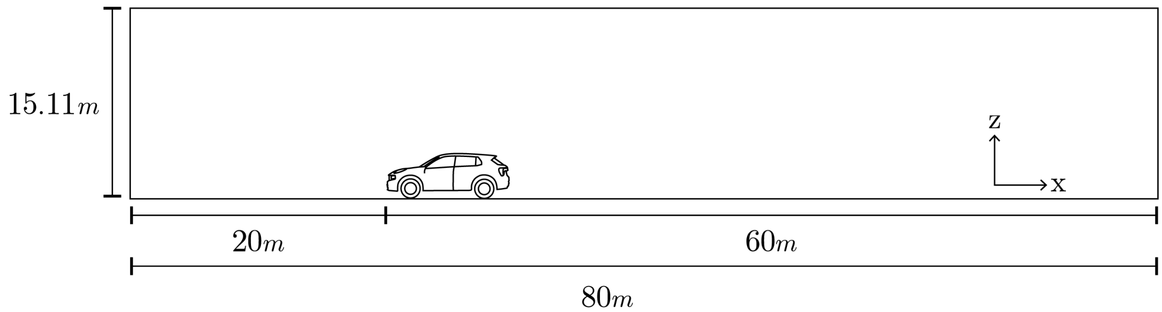

Figure 3.5: Diagram of the virtual wind tunnel.

During the meshing process, different sizing functions were applied wherever necessary. Mesh refinements were applied to the bodies of influence to properly capture the flow in the region closest to the vehicle and also to capture the flow in the wake.

Additionally, the grid has been refined in the wheels and the interfaces used both for the MRF and the SM cases. In these refinement zones, the max cell size is between $2mm \sim 4mm$ with a growth rate of 1.4, a first aspect ratio of 5 and a feature angle of 30. With the mentioned mesh sizing, the interfaces were meshed capturing every detail. Thus reducing the number of potential bad cells.

On the vehicle's body a prism layer is added to solve the near wall gradient. The prism layer is essential to predict the flow more accurate since the highest gradients are located near the wall. For all the cases in this study, the number of layers was set as per CEVT's given script.

As a result, the final cell count is inside the range of 100 to 110 million elements depending on the level of detail captured on the wheels and the interfaces. Figure 3.6 shows a clip at $y = 0$ plane of the final mesh.

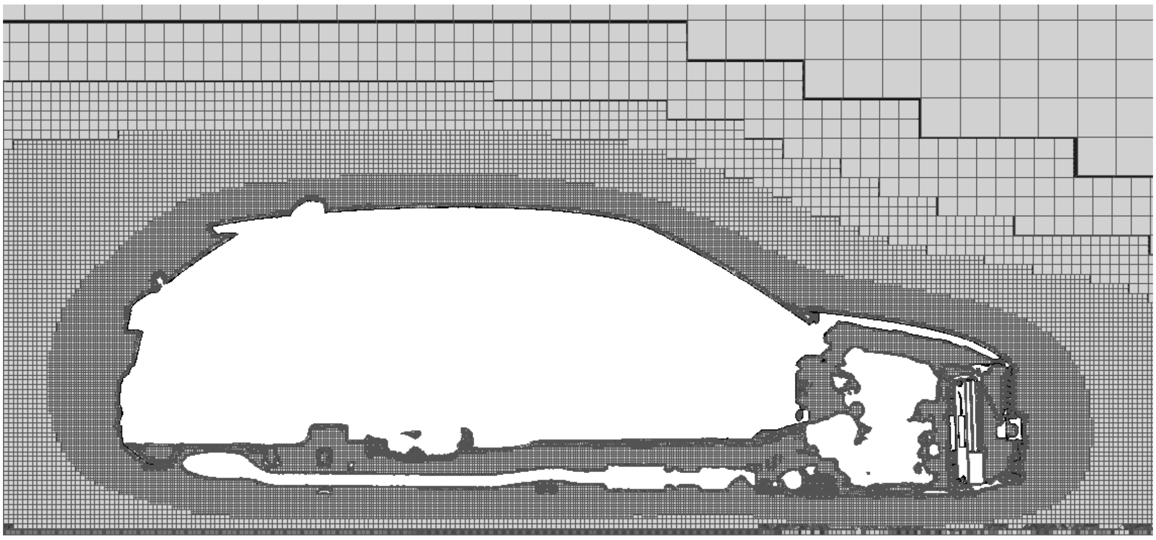

Figure 3.6: Clip at $y = 0$ plane of the final mesh.

3.4 Boundary Conditions

The CFD simulation represents a vehicle moving straight forward (zero yaw) with a velocity of $100\,km/h$. The ground plane is set as a moving wall with a tangential velocity of $100\,km/h$ in x-direction. Moreover, the inlet is set as a velocity inlet boundary with the same velocity magnitude and direction as the ground plane. The outlet is set as a pressure outlet, with a pressure value of $101325\,Pa$ (atmospheric pressure). Lastly, the sidewalls and roof are given a symmetrical boundary. Table 3.1 compiles all the boundary conditions and the physics defined.

The simulations are performed in ANSYS Fluent Solver 19.0. The turbulence model for the steady run is a generalized $k - \omega$ (GEKO-model) and a hybrid RANS-LES model SBES for the unsteady part. A comprehensive explanation on the turbulence models can be found in section 2.5. The values used for the different GEKO-model coefficients were taken from CEVT's scripts.

Table 3.1: Virtual tunnel boundary conditions.

Boundary	Condition	Value
Inlet	Velocity Inlet	100 $[km/h]$
Outlet	Pressure Outlet	101325 $[Pa]$
Sidewalls	Symmetry Wall	-
Ground	Moving Wall	100 $[km/h]$
Roof	Symmetry Wall	-

3.5 Wind Tunnel

The experimental data provided by CEVT was performed at the Volvo Cars aerodynamic wind tunnel. The wind tunnel at Volvo is of the slotted wall closed loop type with a test sectional area of $27\,m^2$. Moreover, the turntable is equipped with a complete moving ground system (five belt system) and a boundary layer control system (BLCS).

In the wind tunnel, each wheel of the vehicle rests on a moving belt, also known as a wheel drive unit (WDU), to replicate the wheel motion. Furthermore, the vehicle is mounted on four struts, that together with the WDUs measure are connected to a six component balance to measure the force, which is later converted to dimensionless aerodynamic coefficients [21] [22].

The data given includes C_D, C_{FL} and C_{RL} values for the rims described in figure 3.2. The tests were performed by swapping only the wheels and keeping the rest of the vehicle the same way. Thus, the delta from one test to the next one is due only to the change of wheels. The tests were conducted following standard procedure at Volvo's wind tunnel.

3.6 Case Setup

The motivation for this study is to investigate the correlation between wind tunnel results and CFD when a sliding mesh approach is chosen as the wheel rotation method. This is done by implementing a sliding mesh boundary condition on different rim geometries. The CAD model shown in figure 3.1 was configured to be as similar to the experimental case, some geometrical differences were however not possible to avoid.

The cases have been defined by preserving the exact same model and only swapping the wheels. As specified before, two different CAD models for rims were provided by CEVT. In addition, two modifications on one of the models have been considered as well.

All cases (18" A, half-covered A, fully-covered A and 19" B) were simulated using the same CFD settings. Firstly each case is individually solved using the MRF approach; and thereafter the cases are solved using the sliding mesh approach.

3.7 Calculations

The simulations are performed in ANSYS Fluent 19.0 using a pressure-based solver (for low-speed incompressible flows). GEKO is used as turbulence model for the steady state part. The simulations are assumed to be isothermal-incompressible (as mentioned in section 2); the air density is set to $1.225\,kg/m^3$ and the dynamic viscosity 1.7894×10^{-5}.

For the unsteady part, the GEKO steady state solution is used as an initial flow. The unsteady state part of the simulations is performed using the RANS-LES (GEKO-SBES) turbulence model with a final time-step of $0.00025\,s$ and 2 inner iterations per time-step.

The time-step size is downgraded in order to allow the flow to develop gradually, thereby making the simulation more stable. With the conditions described in this chapter, every unsteady simulation takes approximately $200-250\,h$ CPU hours, with 432 cores allocated per simulation.

It is worth mentioning that the C_D, C_{FL} and C_{RL} values from the unsteady case are averaged over the last four seconds. Additionally, since the unsteady simulations fluctuate with respect to time, the plots and figures shown in the following chapter are constructed as the mean of the specific value (e.g., mean of velocity, pressure, etc).

4

Results

In this chapter, the results are presented in the following way. First, from the wind tunnel data, the different cases are compared by plotting the normalized C_D, C_{FL} and C_{RL} using the 18" A rims as a baseline. From the data provided, one can observe a correlation between drag, front-lift and rear-lift with the rim design. Hence, the trends observed in the wind tunnel results are expected to be replicated in the CFD simulations.

In the second part, the values obtained from the SM and MRF cases are compared to the wind tunnel (WT) values. In this comparison, the values of interest are, again, the change in drag, front-lift and rear-lift due to the change of rims; ΔC_D, ΔC_{FL} and ΔC_{RL} respectively. The comparison is presented such as the deltas from the CFD simulations (SM and MRF) are compared to the deltas from the WT.

As mentioned in the objectives of this report, the aim is to compare the C_D, C_{FL} and C_{RL} deltas of multiple rim designs considering two CFD wheel rotation methods and investigate to what extent it correlates with wind tunnel deltas.

Given that the 18" A rims are the base model of the half-covered and fully-covered versions, the results obtained from the 18" A rims case are used as a reference and thus all the other cases are normalized with respect to the 18" A rims. All simulations are performed following the methodology described in chapter 3.

4.1 Wind Tunnel Data

From the test data provided by CEVT, the C_D, C_{FL} and C_{RL} of all the cases is plotted as an increase or decrease with respect to the 18" Acase. The change in C_D, C_{FL} and C_{RL} is illustrated in figures 4.1, 4.2 and 4.3 respectively. Note that the drag and lift counts are considered as: $0.001 = 1$ count.

The results from the wind tunnel correlate well with the findings by [23] [24] [25] where a decrease in the drag coefficient is observed when the wheel opening are smaller (i.e., the space between the spokes). As a consequence of the reduced wheel opening, the front-lift and rear-lift values increase both for the half-covered and fully-covered.

The half-covered A rim shows a decrease of 4 drag counts with respect to the 18" A rim, the full-covered rims show a decrease of 9 counts. Moreover, the B rims increase of 3 drag counts. Furthermore, the C_{FL} for the half-covered increase by 19 counts while the fully-covered increase by 33 counts with respect to the reference value; on the other hand, the B rims only increased front lift by 3 counts. Similarly, the C_{RL} increased 9 counts for the half-covered and 13 for the full-covered; whilst, the B rims show almost no change at all.

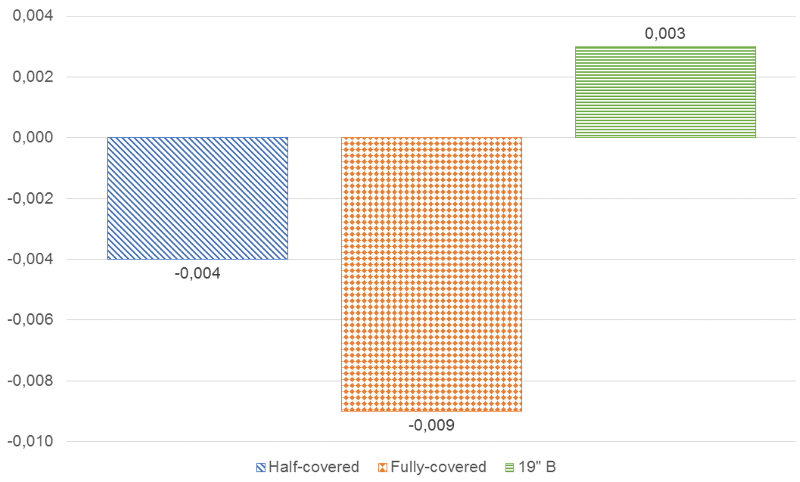

Figure 4.1: Change in C_D from the wind tunnel data.

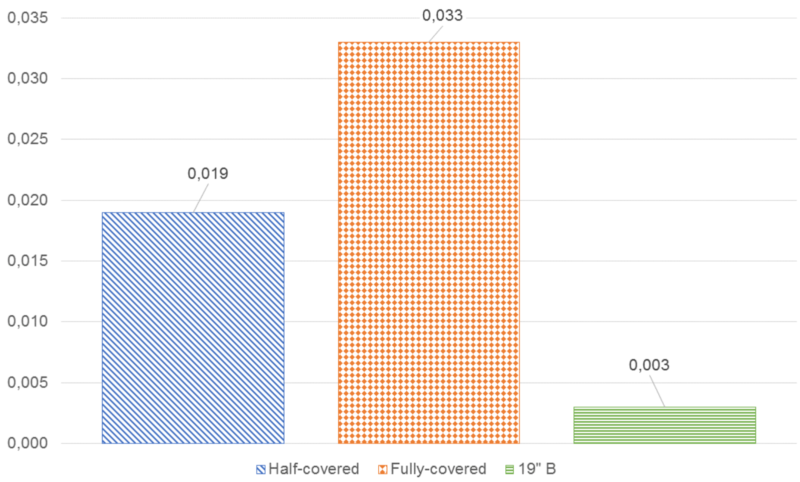

Figure 4.2: Change in C_{FL} from the wind tunnel data.

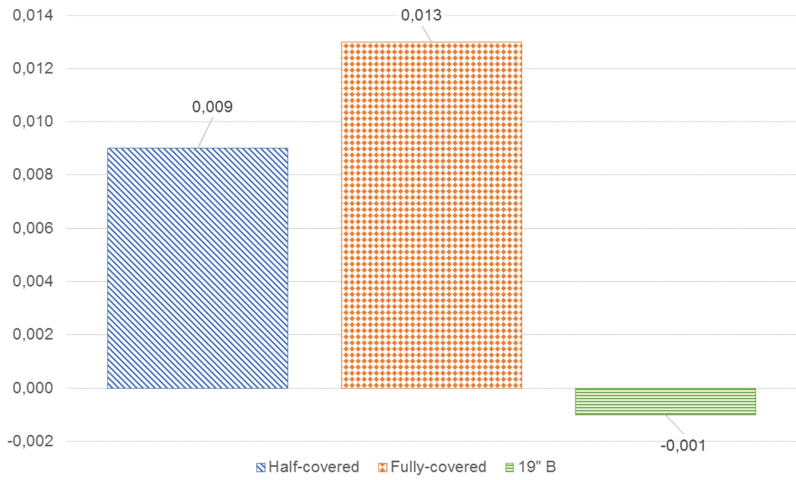

Figure 4.3: Change in C_{RL} from the wind tunnel data.

The data from the wind tunnel serves as a guideline for the computer simulations. The results from CFD simulations are expected to reflect the trends observed in the wind tunnel tests.

4.2 Sliding Mesh vs. MRF

All cases included in this section are averaged over the last four seconds of flow-time. The figures illustrate the deltas from the WT tests, MRF and SM simulations. In the figures below, the cases compared are half-covered, fully-covered and B vs. A. The values shown are calculated as follows.

$$\Delta C_D = C_{D_{a,b,c}} - C_{D_A} \tag{4.1}$$

$$\Delta C_{FL} = C_{FL_{a,b,c}} - C_{FL_A} \tag{4.2}$$

$$\Delta C_{RL} = C_{RL_{a,b,c}} - C_{RL_A} \tag{4.3}$$

Where the subscript a, b, c correspond to half-covered, fully-covered and B respectively. Additionally, a number of post-processed figures are included to further understand the changes in the coefficients.

4.2.1 18" Half-covered *A* Rims vs. 18" *A*

Figures 4.4, 4.5 and 4.6 illustrate the change in drag, front-lift and rear-lift (ΔC_D, ΔC_{FL} and ΔC_{RL}) correspondingly.

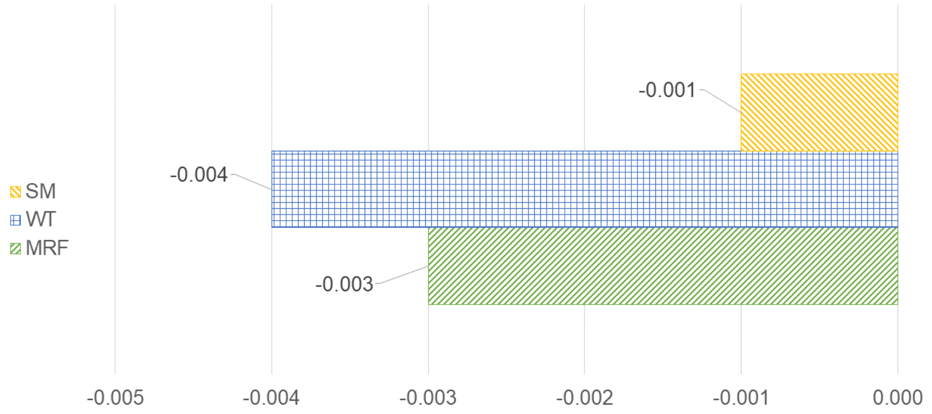

Figure 4.4: Change in C_D (ΔC_D) A vs. half-covered comparison from the wind tunnel data, MRF and SM.

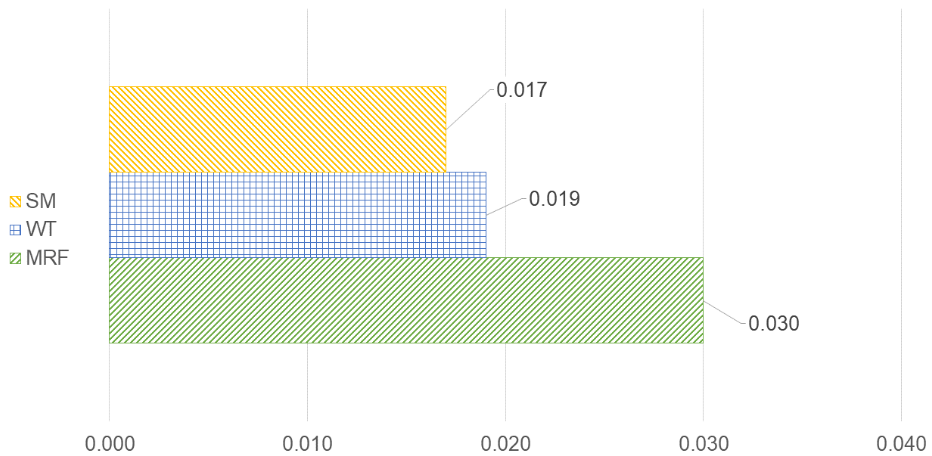

Figure 4.5: Change in C_{FL} (ΔC_{FL}) A vs. half-covered comparison from the wind tunnel data, MRF and SM.

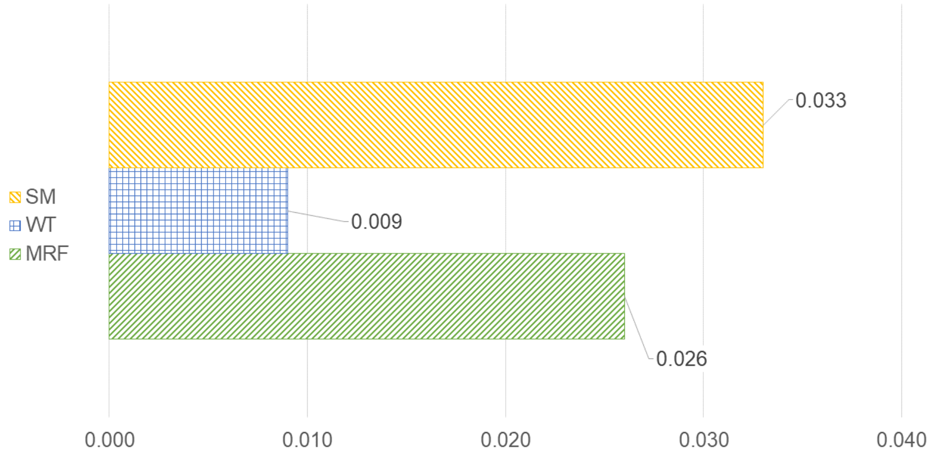

Figure 4.6: Change in C_{RL} (ΔC_{RL}) A vs. half-covered comparison from the wind tunnel data, MRF and SM.

As observed from the WT test results, covering partially the openings of the rim has an effect on the drag; the results from the MRF and SM simulations show the same trend observed from the WT delta, where the half-covered rims decrease the drag slightly. For the MRF case, there is a drag reduction of three counts while for the SM case the reduction is only one count.

To understand where the changes in drag and lift are coming from, it is of interest to plot the cumulative drag and lift (C_D and C_L) along the length of the vehicle. From figure 4.7, one can observe that the configuration with the half-covered rims has a small drop in drag, particularly starting right before the front wheels. This drop in drag is consistently carried along the vehicle. Nevertheless, notice how the slope of the curve corresponding to the half-covered case increases more at the rearmost portion of the vehicle. Thus, the resulting difference is of one count.

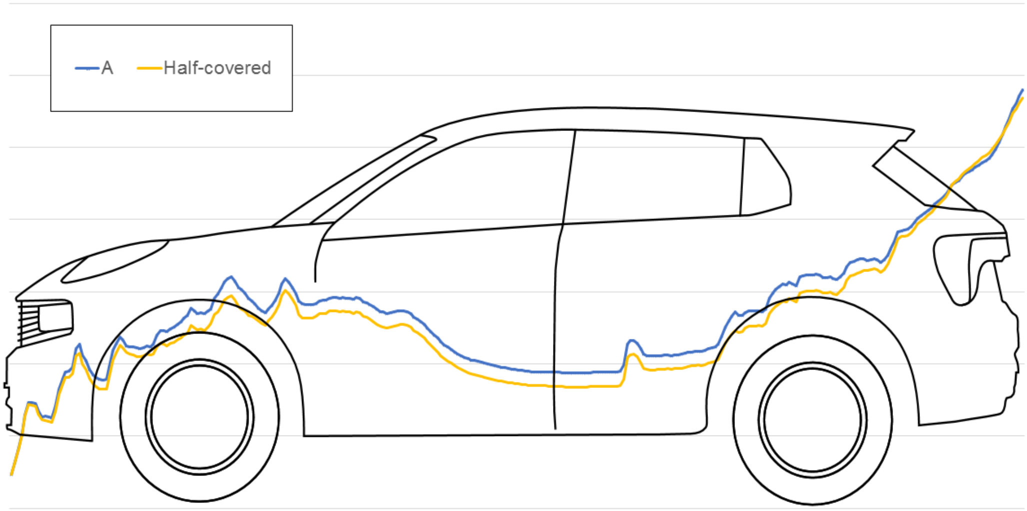

Figure 4.7: Cumulative drag coefficient (C_D) for *A* and half-covered along the length of the vehicle.

In the same manner, the lift coefficient is plotted against the length of the vehicle. The lift coefficient curves diverge right before the front wheelhouse, where the curve for the half-covered case grows significantly more compared to the *A* rims curve. As seen in figures 4.5 and 4.6, the lift coefficient is slightly higher in the half-covered case. Which is confirmed by the cumulative lift curve.

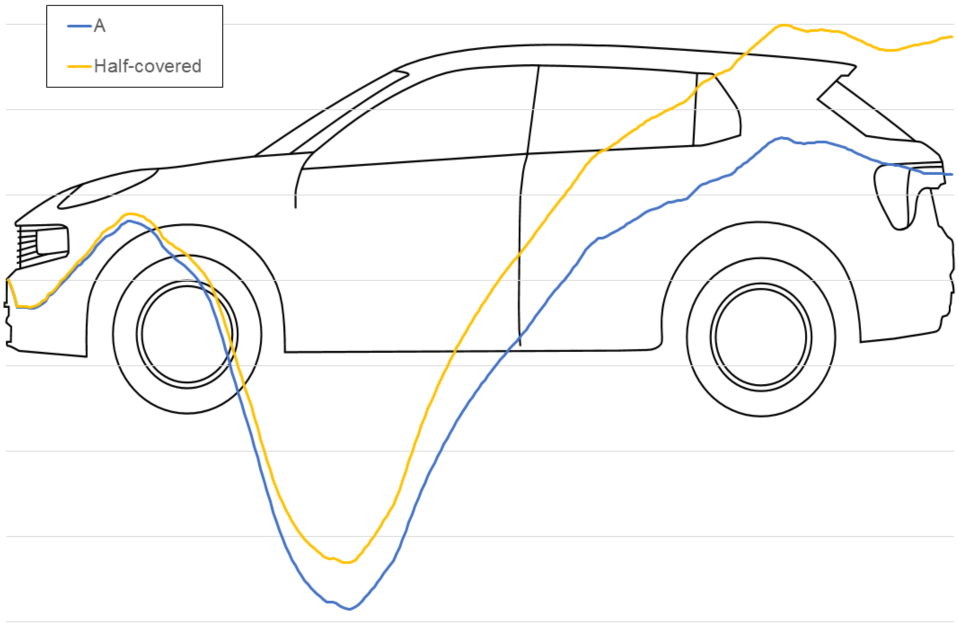

Figure 4.8: Cumulative lift coefficient (C_L) for *A* and half-covered along the length of the vehicle.

To understand the changes in drag and lift coefficients, a number of post-processed figures are included below.

Figures 4.9 and 4.10 show a plane at the middle and 500mm behind the front axle respectively. From the figures, notice that the *A* rims shows three separate wakes are obtained, whereas in the half-covered case, only two wakes are shown. The wake at the bottom is described by [11] as the *jetting* effect. As observed in the figure, this phenomenon is slightly stronger in the half-covered case.

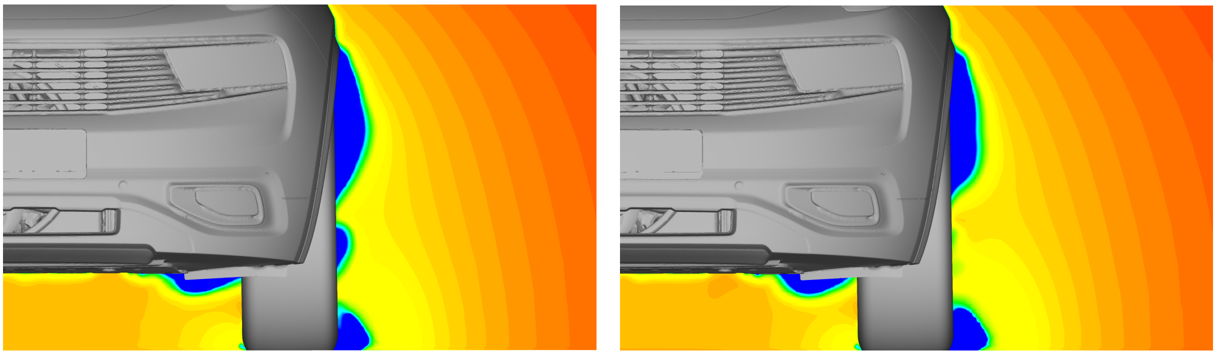

(a) 18" A. (b) 18" half-covered.

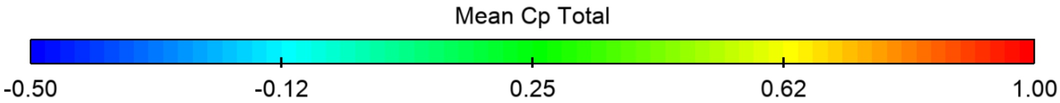

Figure 4.9: Mean total pressure ($C_{P_{tot}}$) at xz-plane at the middle of the front axle for A vs. half-covered.

The wake created at the contact patch is carried downstream until it dissipates. From figure 4.9, one can observe the again three vortexes in the A case (a) and two in the half-covered case (b). Furthermore, notice the wake at the top of the wheelhouse, the wake in (b) is slightly bigger, as the open area in the rim is less, the balance between air exiting through the spokes and through the gap between the tyre and the wheelhouse shifts, and thus, more air exits through the wheelhouse opening creating a larger wake.

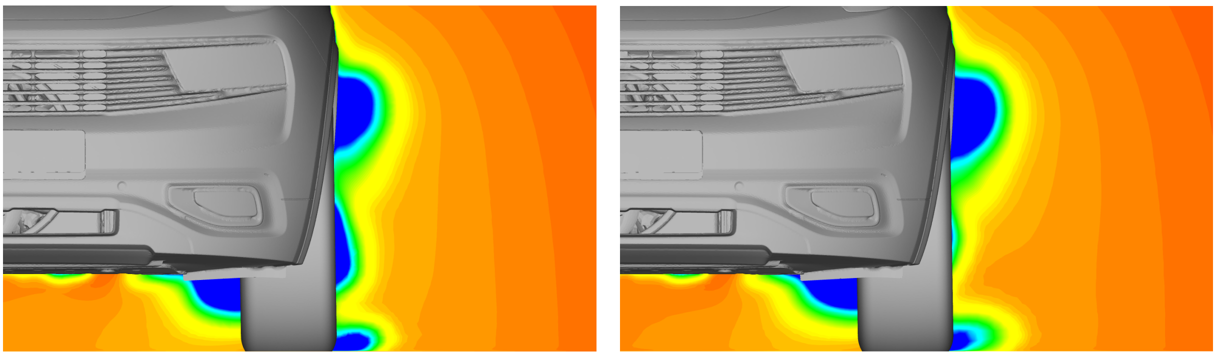

(a) 18" A. (b) 18" half-covered.

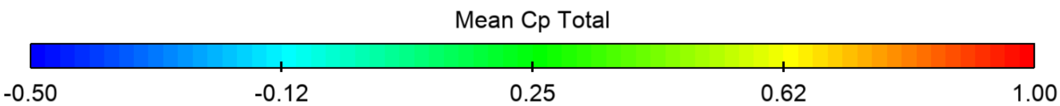

Figure 4.10: Mean total pressure ($C_{P_{tot}}$) at xz-plane 500mm behind the middle of the front axle for A vs. half-covered.

The turbulent flow structure from the wheels is better explained by looking at figures 4.11 and 4.12. The figures shows an isosurface of the mean total pressure coefficient ($C_{P_{tot}} = 0$) for both cases. From the figures, one can observe similarities; the upper and lower (at the contact patch) vortexes are present in both cases, however, for the half-covered (b) the middle vortex is significantly smaller, thus the local pressure losses are less compared to the *A* (a) case.

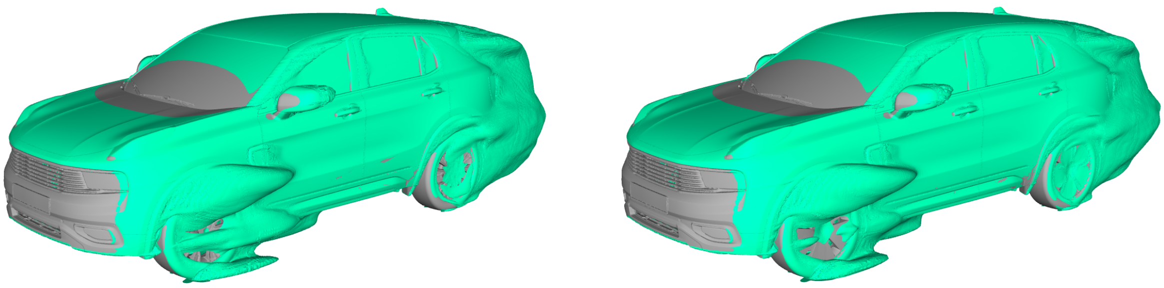

(a) 18" *A*. **(b)** 18" half-covered.

Figure 4.11: Isosurface mean total pressure coefficient ($C_{P_{tot}} = 0$) front isometric view for *A* vs. half-covered.

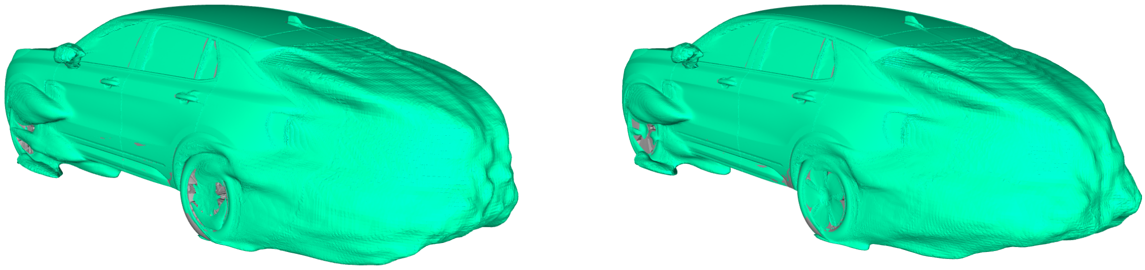

(a) 18" *A*. **(b)** 18" half-covered.

Figure 4.12: Isosurface mean total pressure coefficient ($C_{P_{tot}} = 0$) rear isometric view for *A* vs. half-covered.

Furthermore, the distribution of the pressure coefficient at the base is illustrated in figure 4.13. From the figure, one can observe a small drop in base pressure as a result of closing partially the original rim; particularly at the region between the tail lamps. This drop in base pressure is odd given that the half-covered configuration has a lower C_D and thus the base pressure should be, in theory, larger compared to the *A* case.

The change in base pressure could explain why there is only a drag count difference; a decrease in drag at the front could be countered by an increase at rear wake. A delta of one count is difficult to pinpoint to a specific region of the car. Typically, different rims will not only change the flow locally, but they will affect the overall aerodynamics and thus an increase in drag in one region could be the result of the flow behaviour in a different region.

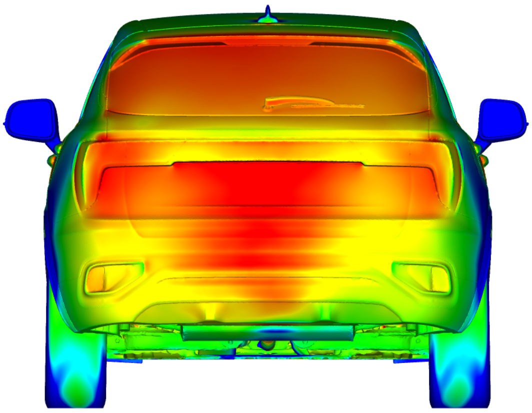

(a) 18" *A*.

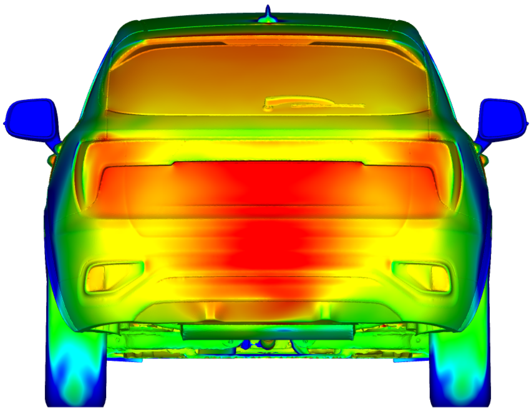

(b) 18" half-covered.

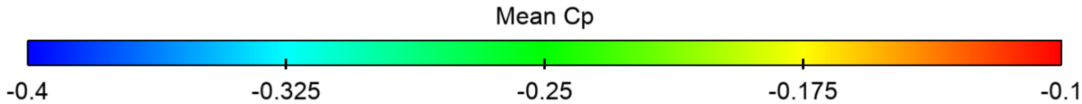

Figure 4.13: Base pressure coefficient distribution for *A* vs. half-covered.

As seen in figures 4.5 and 4.6, the CFD simulations follow the trend observed from the WT, where the front-lift and rear-lift increase as a result of the reduced wheel opening. Once again, the increase in front-lift is most likely because the restricted flow through the wheel spokes thus pressurizing the wheelhouse, thereby increasing the lift.

As mentioned above, covering partially the rim restricts the air flow through the spokes and thus the air is "trapped" in the wheelhouses. As a result of the lesser air going through the spokes, the wheelhouse region pressure increases, and so the front-lift and rear-lift. The restriction of airflow through the spokes, could also affect the brake cooling performance since the "hot" air gets trapped in the wheelhouse region. Figures 4.14 and 4.15 show a bottom view of the front and rear wheelhouses respectively.

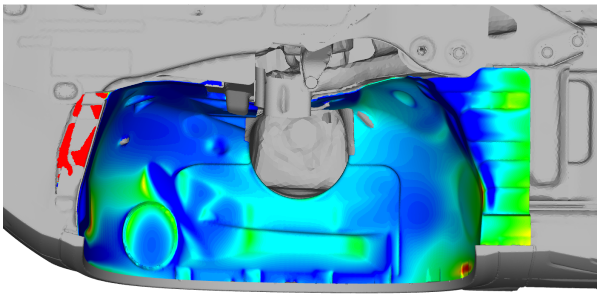

(a) 18" *A*.

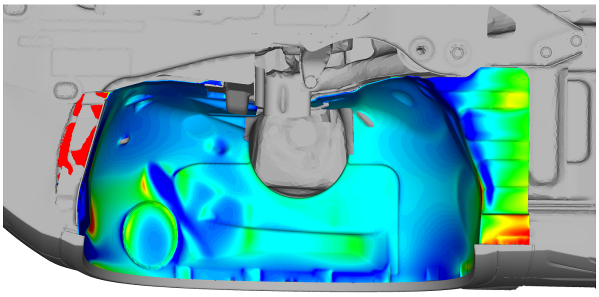

(b) 18" half-covered.

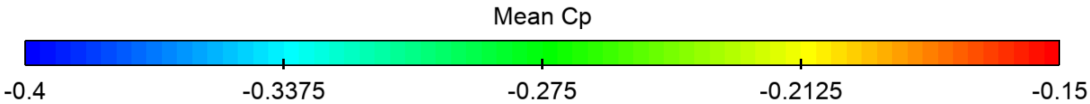

Figure 4.14: Mean pressure coefficient (C_p) front wheelhouse bottom view for *A* vs. half-covered.

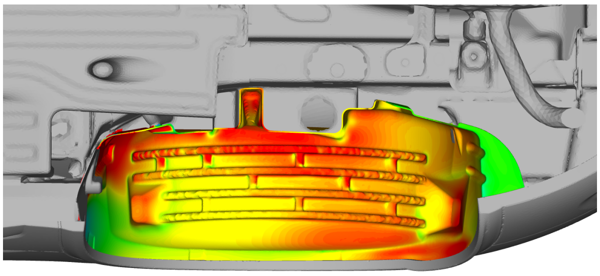

(a) 18" *A*.

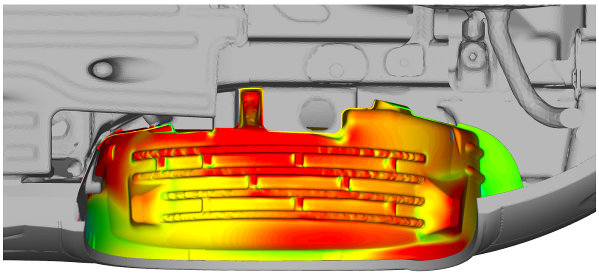

(b) 18" half-covered.

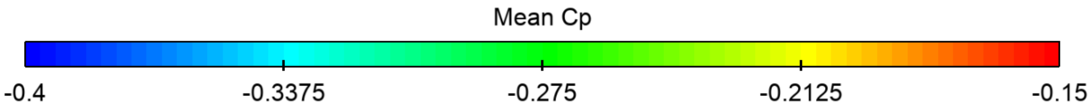

Figure 4.15: Mean pressure coefficient (C_p) rear wheelhouse bottom view for *A* vs. half-covered.

From the figures above, the half-covered case (b) shows an increase in pressure coefficient in both wheelhouses, which correlates well with the deltas observed in 4.5 and 4.6.

4.2.2 18" Fully-covered *A* Rims vs. 18" *A*

Figures 4.16, 4.17 and 4.18 illustrate the change in drag, front-lift and rear-lift (ΔC_D, ΔC_{FL} and ΔC_{RL}) correspondingly. In this instance, the results are unexpected. Opposite to what was observed in the WT results, both CFD simulations show an increase in drag when going from the 18" *A* rims to the 18" fully-covered. Furthermore, the SM case fails to predict the increase in the front-lift and rear-lift observed in the WT.

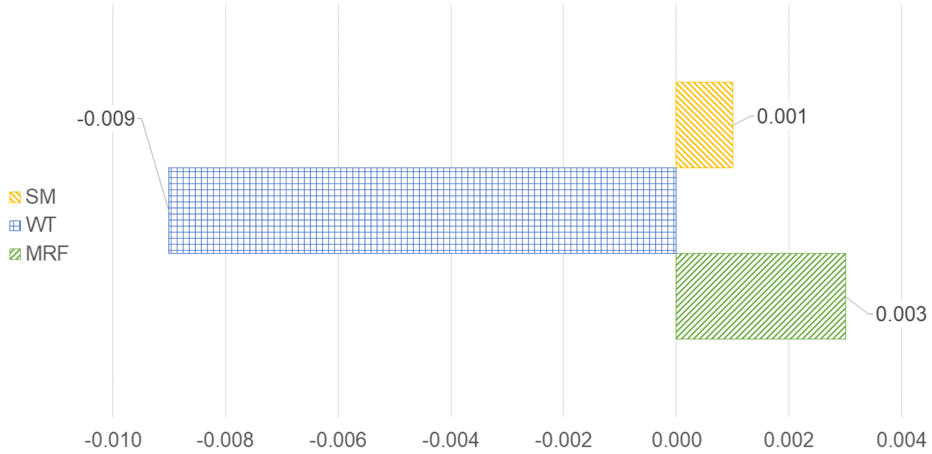

Figure 4.16: Change in C_D (ΔC_D) A vs. fully-covered comparison from the wind tunnel data, MRF and SM.

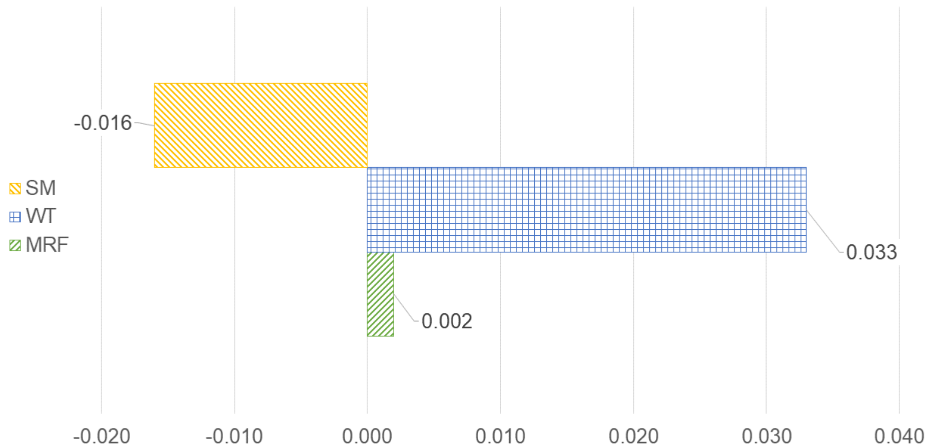

Figure 4.17: Change in C_{FL} (ΔC_{FL}) A vs. fully-covered comparison from the wind tunnel data, MRF and SM.

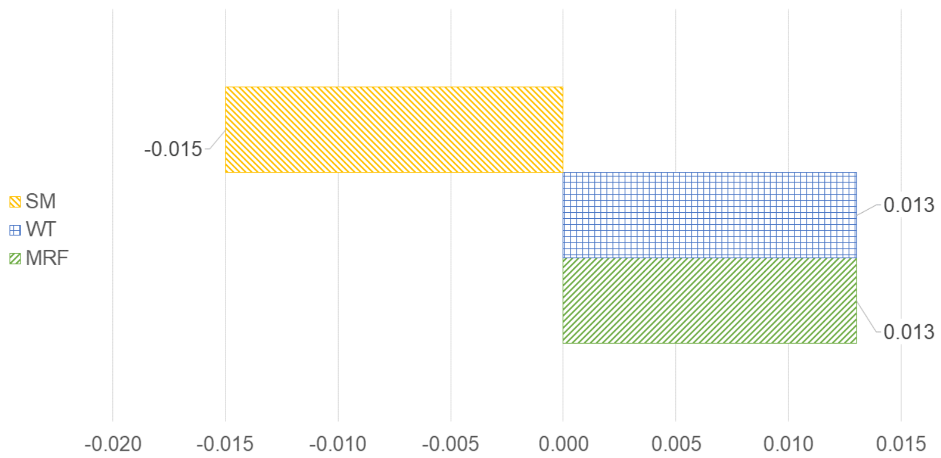

Figure 4.18: Change in C_{RL} (ΔC_{RL}) A vs. fully-covered comparison from the wind tunnel data, MRF and SM.

When looking at the cumulative drag coefficient in figure 4.19, one can observe that the curve corresponding to the fully-covered case has a lower accumulated drag value compared to the A up until the end of the front wheelhouse. Both curves follow a similar profile despite the smaller spikes at the rear wheel. In this case, the fully-covered rim yields an increase of one drag count compared to the A case.

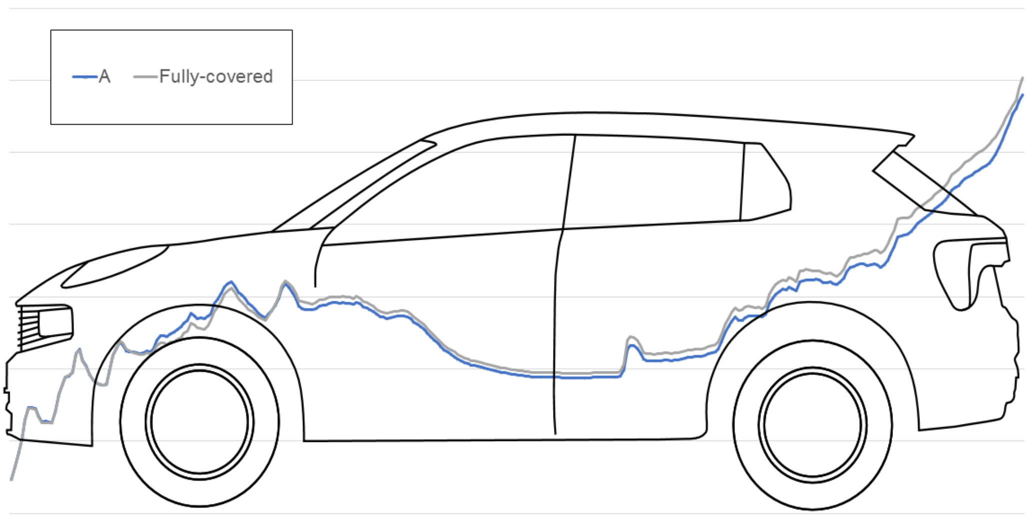

Figure 4.19: Cumulative drag coefficient (C_D) for A and fully-covered along the length of the vehicle.

In addition to the cumulative drag coefficient, the cumulative lift coefficient is also plotted under figure 4.20. From the figure, the biggest change is observed at the rear portion of the vehicle, where the fully-covered case has a bigger drop, thus giving a lower rear-lift value.

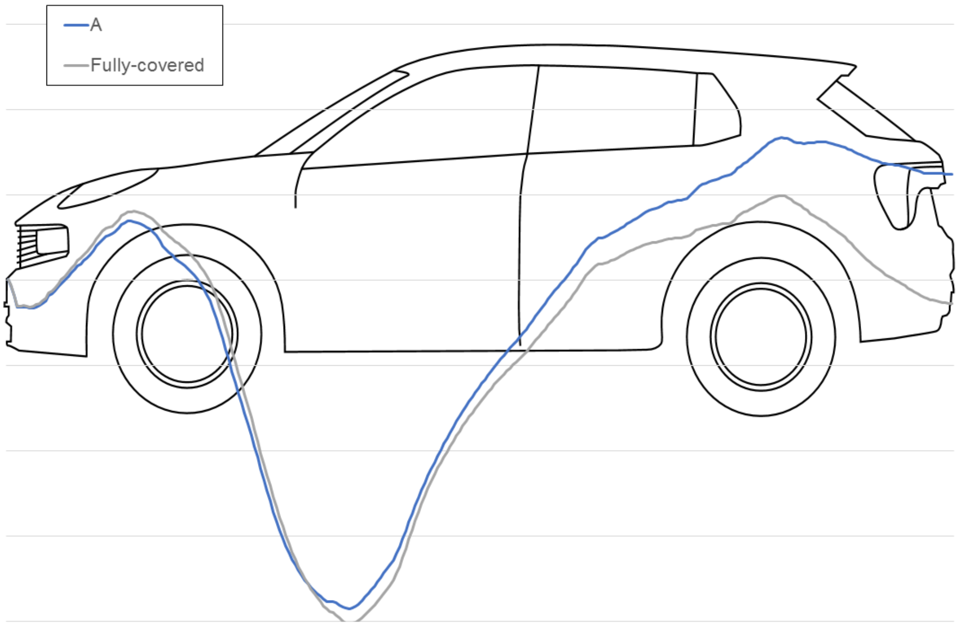

Figure 4.20: Cumulative lift coefficient (C_L) for A and fully-covered along the length of the vehicle.

As mentioned above, according to the results from the SM case, the front-lift and rear-lift decrease when covering up the outer face of the 18" A rims with a flat cover. To further understand why the obtained results deviate from the WT results, a number of figures are included.

Figure 4.21 show a plane at the middle (a)-(b) and 500mm behind the front axle (c)-(d).

Similarly to the half-covered case, the fully-covered case (b) also has two separate wakes. In this case, the wake at the contact patch is significantly larger compared to the one observed in the A case (a), which implies larger losses.

Despite the bigger losses at the contact patch in the fully-covered case, the planar surface of the flat rim has a significant effect on flow separation, it encourages the flow to reattach right after it separates at the tyre shoulder, and thus a smoother flow is observed at the center-height of the rim as observed in figure 4.21 (b) and (d).

These effects are better distinguished in figures 4.22 and figure 4.23. The figures show an isosurface of constant total pressure $C_{p_{tot}} = 0$ front and rear isometric views respectively.

In figure 4.22, the upper and lower vortexes are visible in both cases; similarly to the half-covered case, the middle wake is not present in the fully-cover rim case. The larger wake at the contact patch seen in 4.21 (b) is appreciated easily in this figure. Where the wake is significantly larger and it dissipates into the underbody.

From a rear view, in figure 4.23 the biggest difference is seen behind the rear wheels, where in (b) exhibits a smaller wake behind the rear wheel at the contact patch. Also, the flat surface of the rear rim in (b) shows smaller separation, specially in the lower half of the rim.

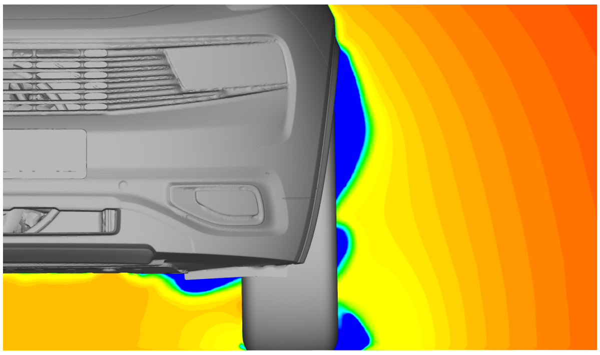

(a) 18" A middle front axle.

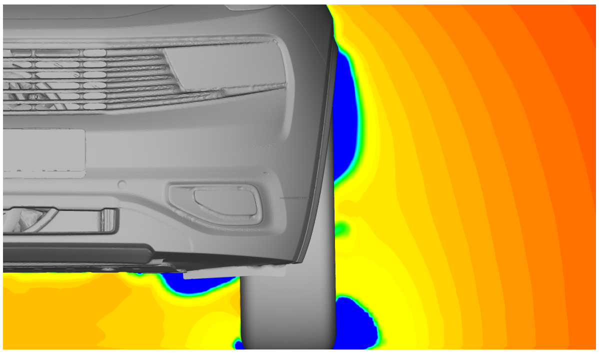

(b) 18" fully-covered middle front axle.

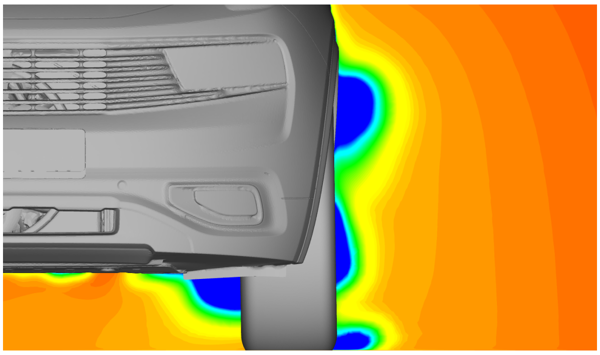

(c) 18" A 500mm behind front axle.

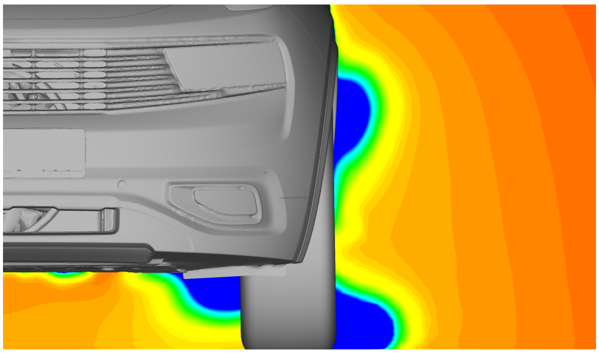

(d) 18" fully-covered 500mm behind front axle.

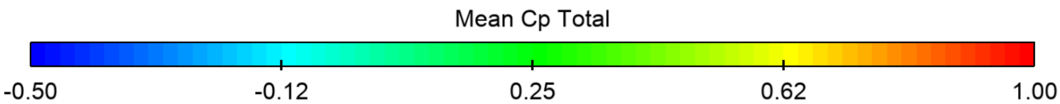

Figure 4.21: Mean total pressure coefficient xz-plane at the middle and 500mm behind of the front axle for A vs. fully-covered.

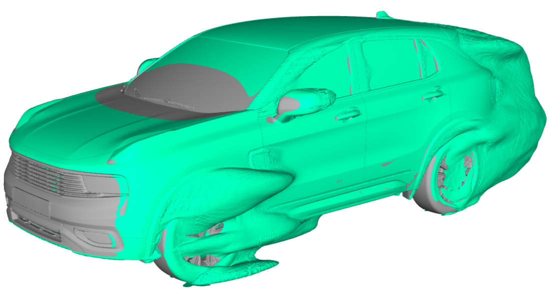

(a) 18" A.

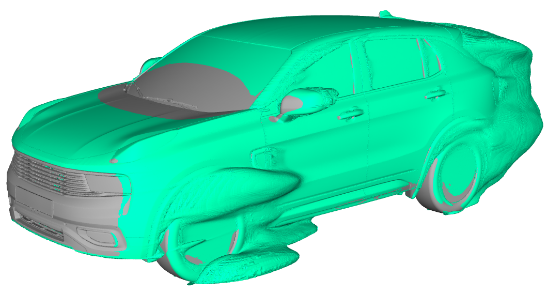

(b) 18" fully-covered.

Figure 4.22: Isosurface mean total pressure coefficient ($C_{P_{tot}} = 0$) front isometric view for A vs. full-covered.

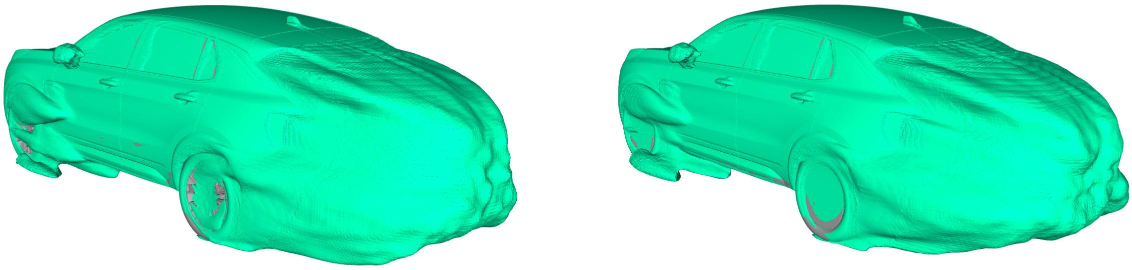

(a) 18" A. **(b)** 18" fully-covered.

Figure 4.23: Isosurface mean total pressure coefficient ($C_{P_{tot}} = 0$) rear isometric view for A vs. full-covered.

Figure 4.24 shows the mean base pressure coefficient for the A and fully-covered rims. From the figure, one can notice a slightly higher pressure on the fully-covered case (b), particularly on the bumper region of the vehicle, where the base pressure widens. Furthermore, (b) shows two low pressure spots on the lower outer face of the tyres. These spots indicate a stronger inflow coming from the vortex formed at the rear of the rear tyres. Figure 4.25 shows a plane behind the rear tyre ($x = 4.9m$) colored by the mean lateral velocity. From the figure (b), one can notice the vortex created behind the rear wheel which moves towards the rear wake.

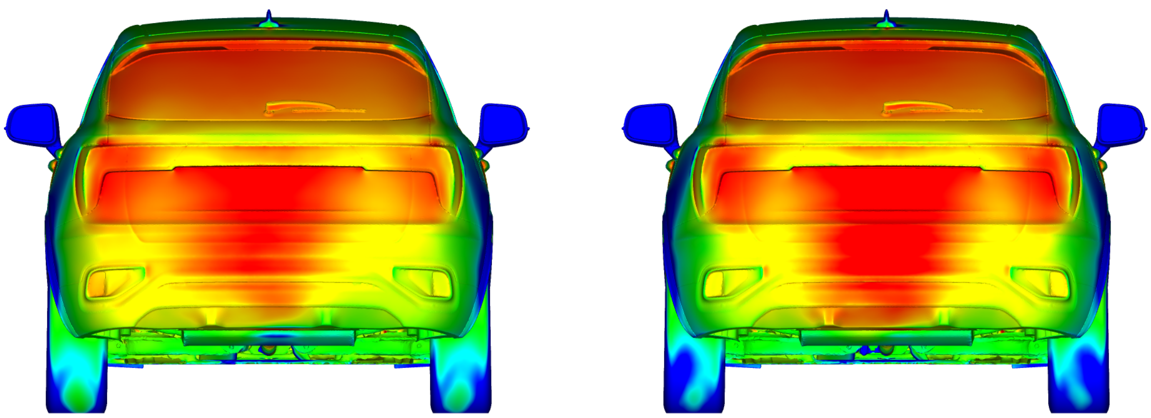

(a) 18" A. **(b)** 18" fully-covered.

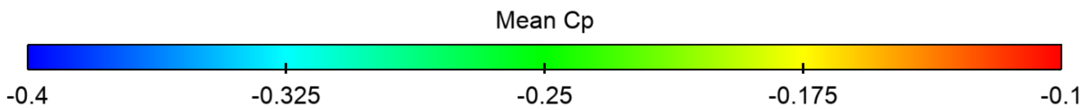

Figure 4.24: Base pressure coefficient distribution for A vs. fully-covered.

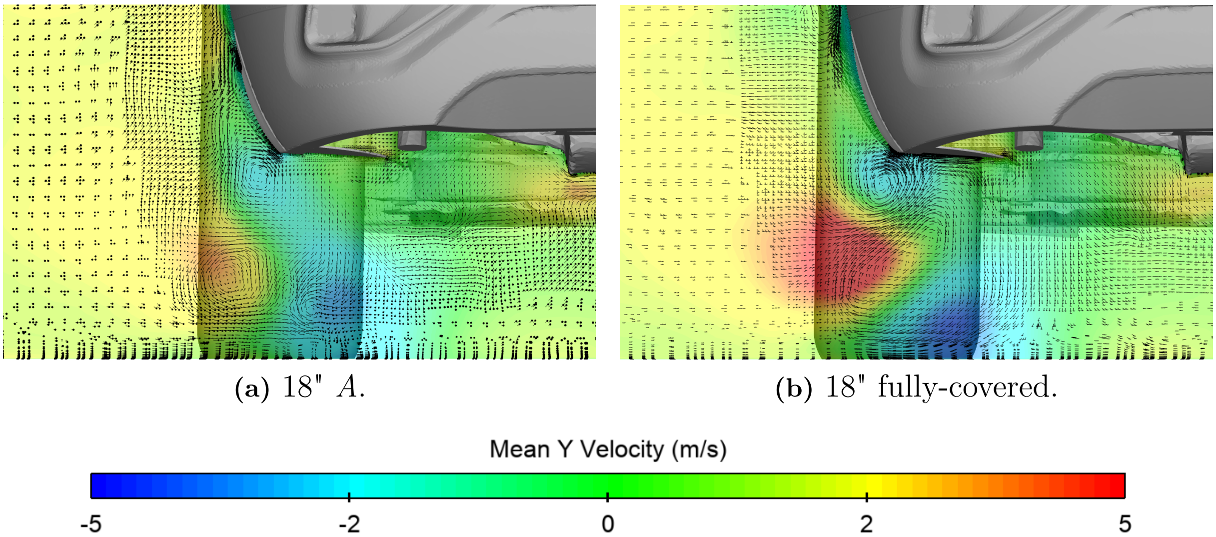

Figure 4.25: Mean lateral velocity at a plane $x = 4.9m$ for A vs. fully-covered.

In contrast to the effects seen in the half-covered case, the fully-covered case shows an unexpected decrease in front-lift and rear-lift. This is illustrated by the decrease in pressure coefficient shown in figures 4.26 and 4.27 for the front and rear respectively.

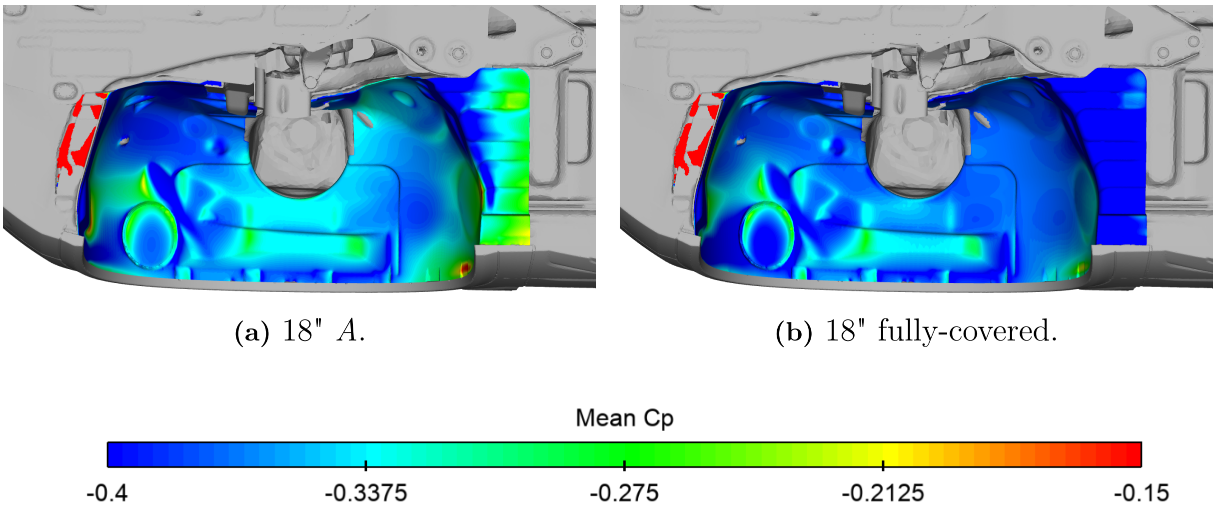

Figure 4.26: Mean pressure coefficient (C_p) front wheelhouse bottom view for A vs. fully-covered.

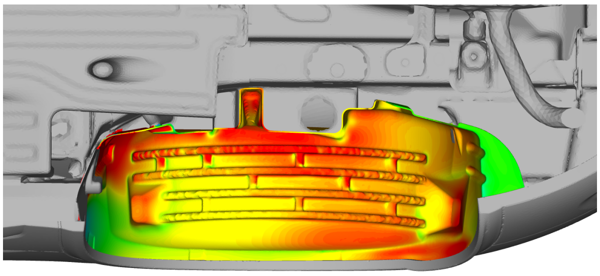

(a) 18" A.

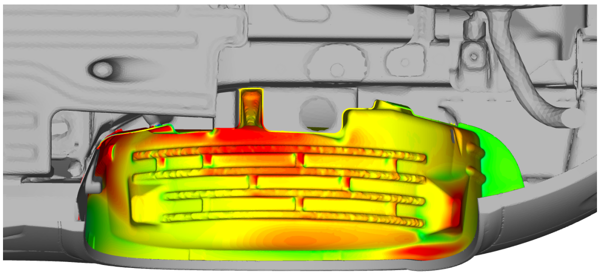

(b) 18" fully-covered.

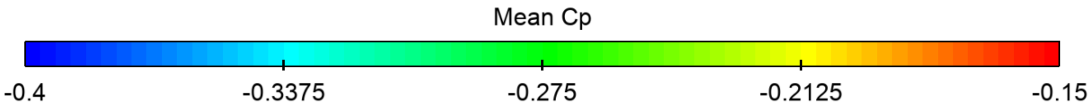

Figure 4.27: Mean pressure coefficient (C_p) rear wheelhouse bottom view for A vs. fully-covered.

4.2.3 19" *B* vs. 18" *A*

Figures 4.28, 4.29 and 4.30 illustrate the change in drag, front-lift and rear-lift (ΔC_D, ΔC_{FL} and ΔC_{RL}) correspondingly.

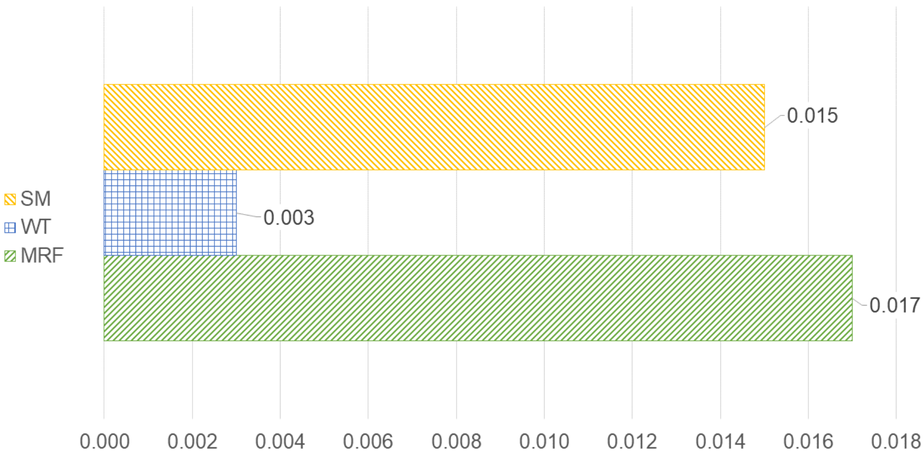

Figure 4.28: Change in C_D (ΔC_D) B vs. A comparison from the wind tunnel data, MRF and SM.

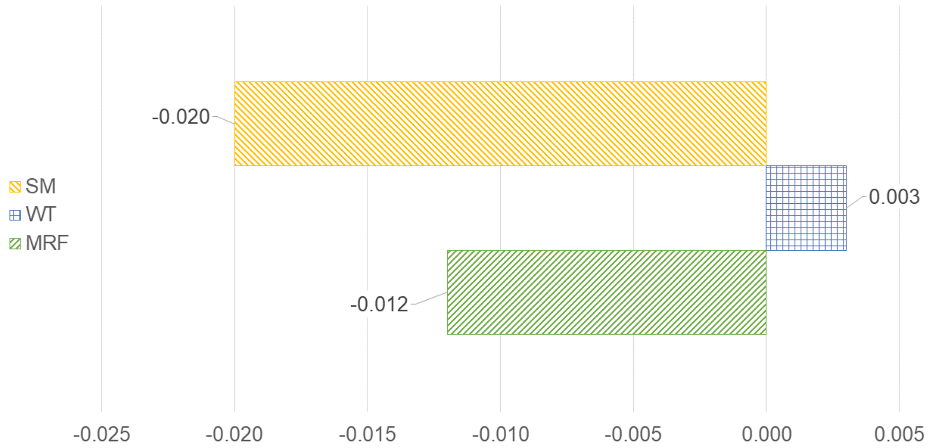

Figure 4.29: Change in C_{FL} (ΔC_{FL}) B vs. A comparison from the wind tunnel data, MRF and SM.

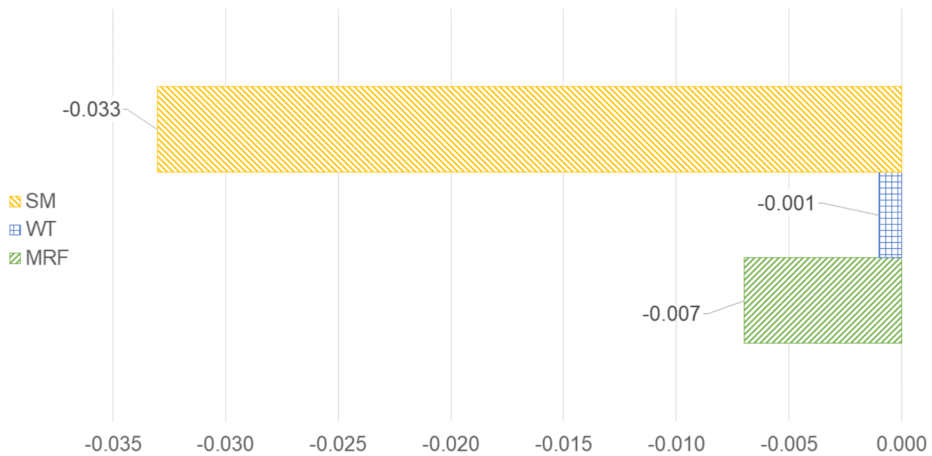

Figure 4.30: Change in C_{RL} (ΔC_{RL}) B vs. A comparison from the wind tunnel data, MRF and SM.

As observed in figure 4.28, both wheel rotation methods predict the increase in drag due to the B rims. Both methods overestimate the drag delta, for the SM case, the drag is overestimated by 12 counts while for the MRF case the value is overestimated by 14 counts.

Furthermore, figure 4.29 and 4.30 show the front-lift and rear-lift deltas. The deltas show that both methods failed to predict the increase in front-lift. Whilst the rear-lift decrease is predicted correctly by both CFD methods, both overestimate significantly the drag reduction.

The cumulative drag coefficient for the B case is plotted in figure 4.31, notice the spike right after the front wheelhouse, which indicates possibly pressure losses due to the front wheel wake; the difference between the two curves is constant along the vehicle.

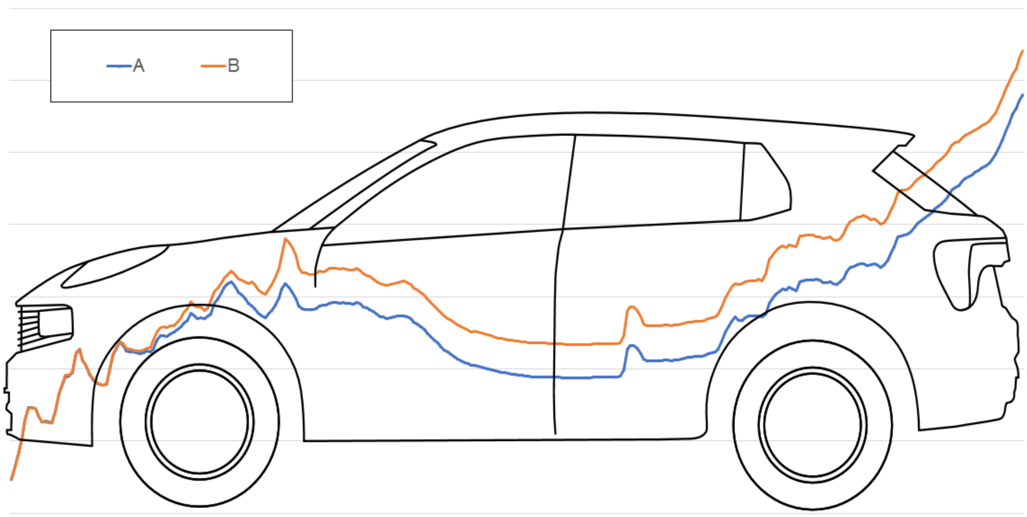

Figure 4.31: Cumulative drag coefficient (C_D) for *A* and *B* along the length of the vehicle.

From figure 4.32, the biggest change is observed, again, at the rear portion of the vehicle, particularly from the middle of the car onward, where the *B*case deviates from the *A* case curve. In addition to this effect, the *B* case shows a steeper drop after the rear wheel. Matching the deltas observed in figures 4.29 and 4.30.

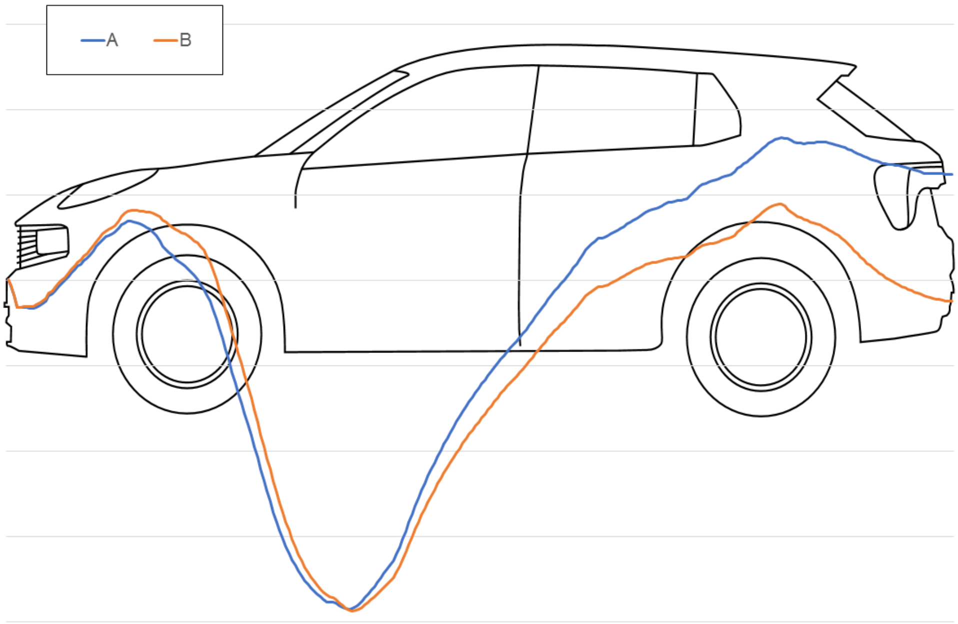

Figure 4.32: Cumulative lift coefficient (C_L) for A and B along the length of the vehicle.

In the same way as the previous cases, plotting the pressure coefficient at the base of the vehicle; one can observe that the B rim has a higher base pressure coefficient despite being the configuration with a higher drag coefficient. Notice also the low pressure spots at the bottom outermost face of the rear tyres. Again, these low pressure spots are the result of the strong inflow coming from behind the rear tyres.

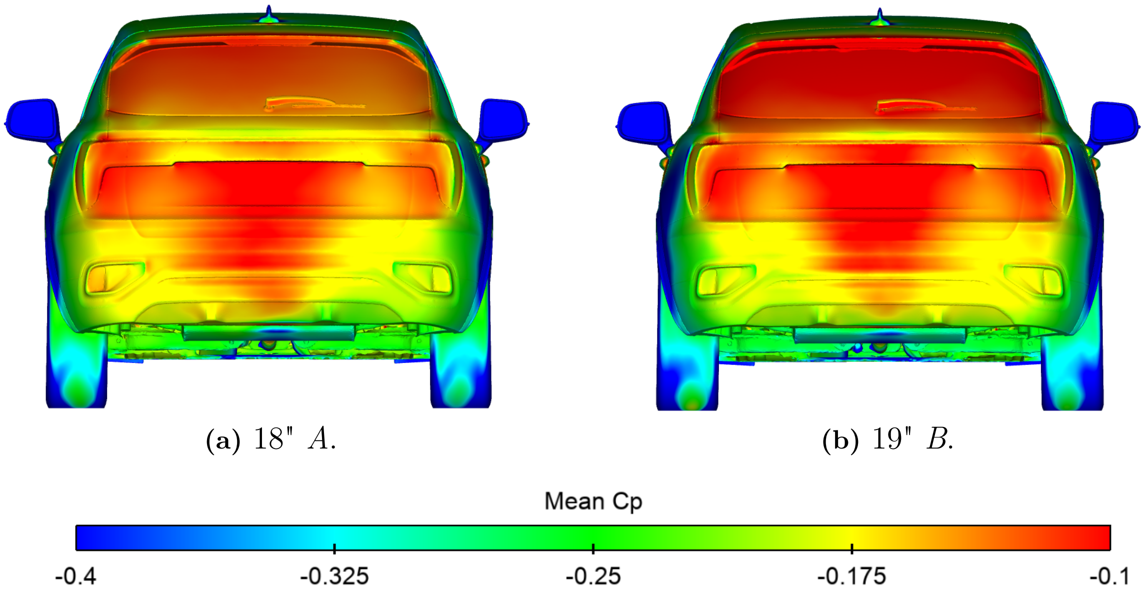

(a) 18" *A*.

(b) 19" *B*.

Figure 4.33: Base pressure coefficient distribution for *B* vs. *A*.

To further comprehend the flow differences, in figures 4.34 and 4.35, one can observe a significant difference in the wake at the front tyre. The *B* case (b), develops a much stronger vortex at the contact patch, this vortex is carried away towards the underbody until it dissipates.

The rear wake from the *B* case (b), has a slightly steeper upwash compared to the *A* case (a). This is probably result of the inflow interacting differently with the lower portion of the rear wake, thus having a different balance with the downwash.

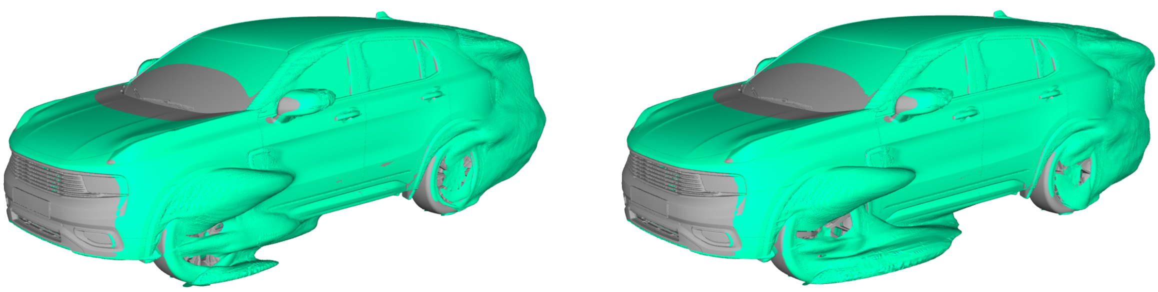

(a) 18" *A*.

(b) 19" *B*.

Figure 4.34: Isosurface mean total pressure coefficient ($C_{P_{tot}} = 0$) front isometric view for *A* vs. *b*.

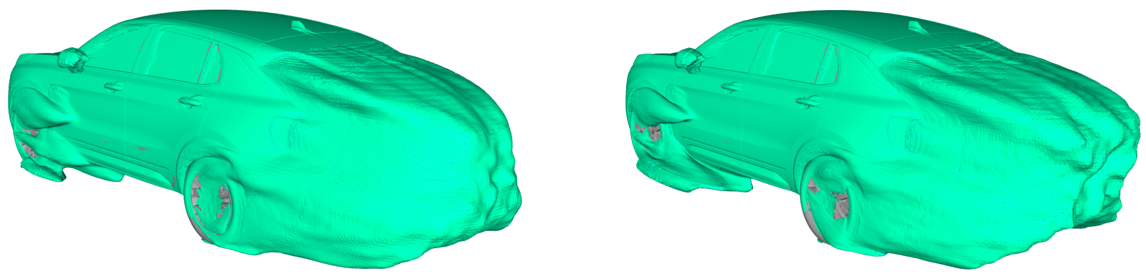

(a) 18" *A*.

(b) 19" *B*.

Figure 4.35: Isosurface mean total pressure coefficient ($C_{P_{tot}} = 0$) rear isometric view for *A* vs. *B*.

The front-lift and rear-lift decrease is observed in figures 4.36 and 4.37 respectively. In the case of the front-lift, both (a) and (b) are very much alike despite the difference of 20 counts. On the other hand, the change in rear-lift is noticeable in figure 4.37, where the pressure at the rear wheelhouse is significantly lower and thus reducing the rear-lift. This observation is also complemented by the cumulative lift coefficient, where the *B* rims show a steeper drop at the rear portion of the vehicle.

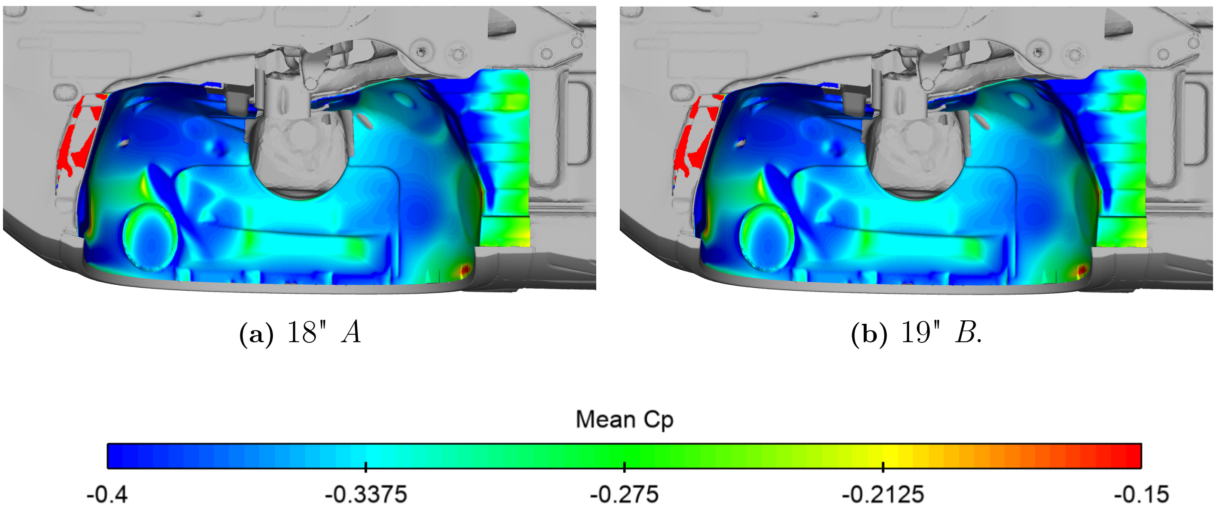

Figure 4.36: Mean pressure coefficient (C_p) front wheelhouse bottom view for *A* vs. *B*.

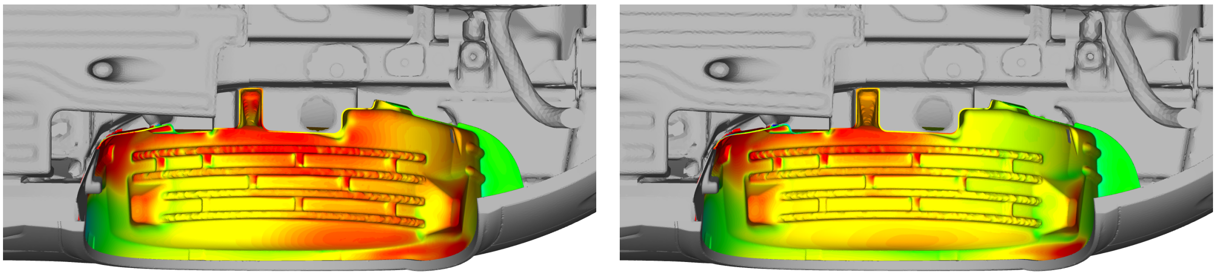

(a) 18" *A*. **(b)** 19" *B*.

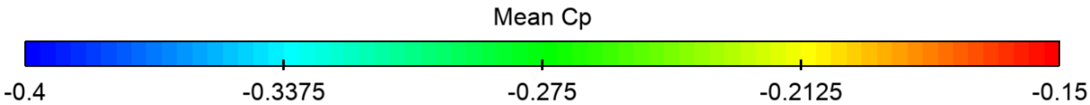

Figure 4.37: Mean pressure coefficient (C_p) rear wheelhouse bottom view for *A* vs. *B*.

To summarize the changes observed, a plot of the cumulative drag and lift of all cases is shown under figures 4.38 and 4.39. From the figures, once again it is noticeable that the differences are spotted at the front and rear wheels. In addition to this, it is also interesting to observe how the different spikes have a positive or negative effect with the rear wake or the underbody, this was seen particularly for the lift, a steep drop after the rear wheel in the case of the fully-covered and *B* rims, whereas the half-covered showed an different interaction with the rear wake.

Surprisingly, the fully-covered case deviate from the trends observed. However, flat rims are known for being challenging to model in CFD simulations and often deliver results outside the uncertainty margins [26] [2] [3] [27].

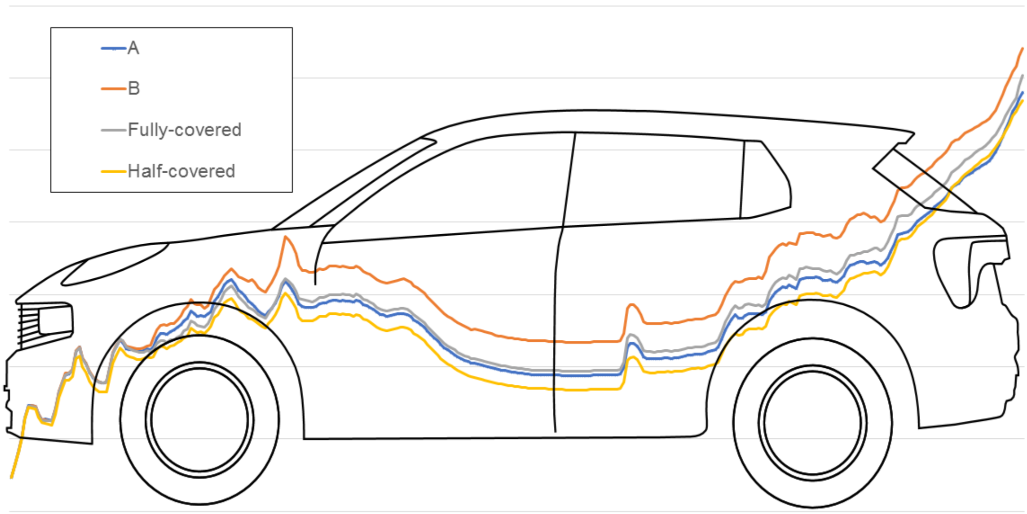

Figure 4.38: Cumulative drag coefficient (C_D) for *A*, half-covered, fully-covered and *B* along the length of the vehicle.

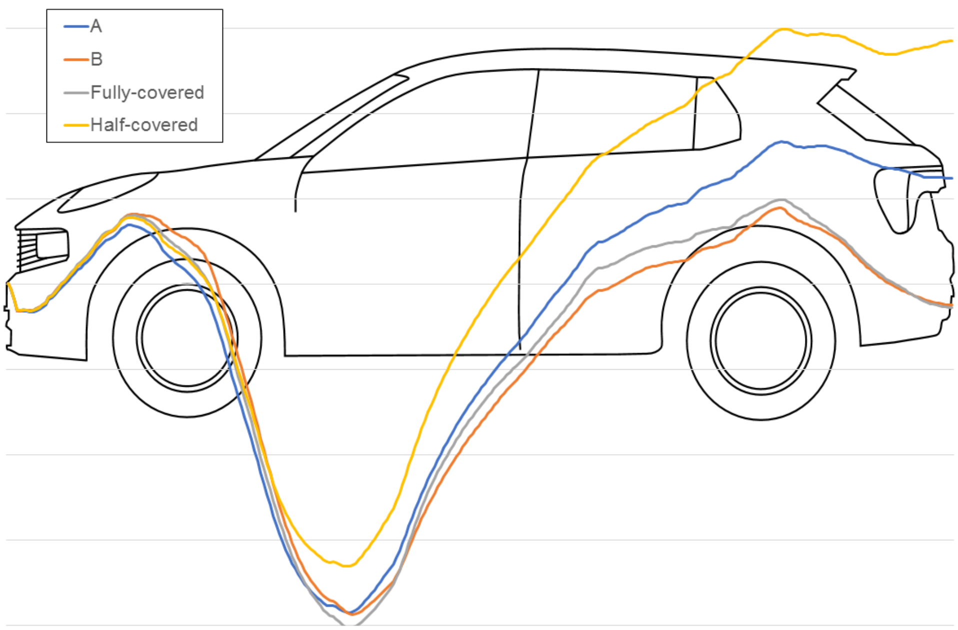

Figure 4.39: Cumulative lift coefficient (C_L) for *A*, half-covered, fully-covered and *B* along the length of the vehicle.

5

Conclusion

From the performed simulations, it is evident that CFD is a valuable tool to keep up with the fast-paced passenger mobility development. Not only allows to evaluate the aerodynamic performance of a vehicle at early stages of its development, but also enables engineers to perform a greater number of virtual tests (CFD simulations) compared to experimental tests (wind tunnel tests). Overall, CFD is used by engineers to do a quick assessment of design variations, it provides comprehensive information in terms of flow visualization and measurements that experimentally are challenging to measure, it enables engineers to simulate different conditions, and last but not least it lowers the development cost associated with design validation.

As described in the background chapter (1.1), wheels account for quarter of the total aerodynamic drag [8] [9] [10]. Thus, wheel design has been of particular interest in many research cases [2] [26]. The exposed area of a rim (i.e., wheel opening) has been also the subject of study [23] [24] [27].

These studies show a strong correlation between a smaller area and lower drag values. However, a complete closed rim has significant drawbacks. For starters, the lift values increase, which in return affect the maneuverability of the vehicle. In general, commercial vehicles have positive lift; Nonetheless if the lift exceeds a given limit, the car could become unstable at higher speed. In addition, flat rims restrict the incoming and outcoming flow, thus reducing the mass flow through the disc brakes and increasing the local pressure inside the wheelhouse.

From the simulated cases, only the half-covered vs. *A* case seem to deliver good predictability, particularly for the drag and front-lift. The fully-covered and *B* cases showed unexpected and/or inaccurate results. Prior studies [26] and [2], found an increase in drag when performing simulations using fully-covered rims; which is the case in this study.

Sliding mesh implementation proved to be significantly challenging. The biggest obstacles were time and know-how; as explained in the theory chapter (see 2.7.3), the sliding mesh cell zones update every time-step and thus making the simulations time dependant (i,e,. transient simulations). In contrast to steady simulations; transient simulations are heavy in terms of computer resources. The computation time increase by 95% approximately compared to an unsteady simulation with MRF as rotation method. Hence, taking significantly more time to reach a solution. The significant increase in computation time constrained, to some degree, the number of cases and thus the amount of data to produce results.

In contrast with the findings from [2] [3] [1] [4] [28], the results from the sliding mesh cases don't show significant improvements over the MRF cases. Nevertheless, it motivates new attempts on tuning the implementation.

5.1 Summary

- Accurate wheel rotation modeling is notably challenging for a number of reasons. For starters, the tyres have complex geometries with a lot of details that affect the flow behaviour and thus the overall aerodynamic performance of a car. Thus, making it hard to compare numerical cases against wind tunnel tests where the tyres are not the same.
- Tyre deformation due to centrifugal and normal loads makes sliding mesh only applicable to the rims.
- Special care should be put in meshing the interfaces for sliding mesh. Many errors are a consequence of poor mesh quality in the interfaces or mesh motion conditions.
- The area around the wheel and inside the wheelhouse is known for its highly unsteady and turbulent flow, which results in many regions prone to separation. The MRF method provides a reasonable correlation to wind tunnel results without compromising the solution time and thus it is applied widely in the automotive industry. However, SM is a method that reassembles the motion of the wheel more accurately, thereby capturing in a better way the flow around the wheel region.
- Given that the sliding mesh interfaces can extend outwards from the rims without producing the negative effects that MRF would produce. A sliding mesh generic interface could be developed and implemented regardless of the rim design. Whereas in MRF, the user must create a specific interface for each case.
- The sliding mesh approach has a lot to offer. Nonetheless, its computational demands limit its use to specific cases. For example, fine tuning a rim or brake disc design. To produce detailed drag and lift values for a specific rim.

5.2 Future Work

A number of different simulations have been left for the future due to lack of time (i.e., unsteady simulations with dynamic meshes are usually very time consuming, requiring even multiple days to finish). Future work concerns detailed implementation of the sliding mesh method, a wider range of cases, a deeper analysis of the method accuracy, and simply curiosity.

The points listed below summarize some ideas to test in the future:

- Perform further studies on the use of sliding mesh versus other methods for wheel rotation modelling.

- Consider overset mesh (also known as "overlapping" mesh) as a wheel rotation method. When used in appropriate cases, overset mesh has the potential to optimize the local cell types and quality, reduce cell count (and, therefore, computation time), or simplify model setup.

- Investigate mesh resolution sensitivity with a especially attention to the interfaces.

- Investigate more carefully the unsteady solution; making sure that the CFL criteria is fulfilled, time-step size and inner iterations per time-step.

- Perform simulations with rotating brakes and static brakes to evaluate the impact in results and computational demands.

- Perform further studies regarding slick tyres versus detailed tyres using sliding mesh as a wheel rotation modelling.

- Further optimize the interfaces to capture only the non axisymmetric parts of the rim. This probably results in less cells inside the sliding mesh zone, thus less moving cells and computational resources needed.

- Carry out more simulations using different rims on the same vehicle with sliding mesh as wheel rotation model.

- Evaluate the impact of averaging over less flow-time.

Bibliography

[1] R. Lewis, M. Cross, and D. Ludlow. *"The influence of rotating wheels on the external aerodynamic performance of a vehicle"*. In *International Vehicle Aerodynamics Conference 2014*, pages 161 – 174. Woodhead Publishing, 2014.

[2] Andrew D'Hooge, Robert B. Palin, S. Johnson, Bradley Duncan, and Joaquin Ivan Gargoloff. *"The Aerodynamic Development of the Tesla Model S - Part 2: Wheel Design Optimization"*. Technical Paper 2012-01-0178, SAE International, 2012. DOI: 2012-01-0178.

[3] Teddy Hobeika and Simone Sebben. *"Tyre Pattern and their Effects on Passenger Vehicle Drag"*. Technical Paper 2018-01-0710, SAE International, 2018. DOI: 2018-01-0710.

[4] Satheesh Kandasamy, Bradley Duncan, Holger Gau, Fabien Maroy, and Alain Belanger. *"Aerodynamic Performance Assessment of BMW Validation Models using Computational Fluid Dynamics"*. Technical Paper 2012-01-0297, SAE International, 2012. DOI: 2012-01-0297.

[5] European Environment Agency (EEA). *"Greenhouse Gas Emissions From Transport"*. URL: https://www.eea.europa.eu/data-and-maps/indicators/transport-emissions-of-greenhouse-gases/transport-emissions-of-greenhouse-gases-10.

[6] Wolf-Heinrich Hucho. *"Aerodynamics of Road Vehicles"*. SAE International, Warrendale, USA, 4th edition, 1998.

[7] Thomas Schuetz. *"Aerodynamics of Road Vehicles"*. SAE International, Warrendale, USA, 5th edition, 2016.

[8] Jochen Wiedemann. *"The Influence of Ground Simulation and Wheel Rotation on Aerodynamic Drag Optimization - Potential for Reducing Fuel Consumption"*. Technical Paper 960672, SAE International, 1996. DOI: 960672.

[9] E. Mercker and N. Breuer. *"On the Aerodynamic Interference Due to the Rolling Wheels of Passenger Cars"*. Technical Paper 910311, SAE International, 1991. DOI: 910311.

[10] G. Wickern, K. Zwicker, and M. Pfadenhauer. *"Rotating Wheels - Their Impact on Wind Tunnel Test Techniques and on Vehicle Drag Results"*. Technical Paper 970133, SAE International, 1997. DOI: 970133.

[11] Alexander Wäschle. *"The Influence of Rotating Wheels on Vehicle Aerodynamics – Numerical and Experimental Investigations"*. Technical Paper 2007-01-0107, SAE International, 2007. DOI: 2007-01-0107.

[12] Christoffer Landström, Lennart Löofdahl, and Tim Walker. *"Detailed Flow Studies in Close Proximity of Rotating Wheels on a Passenger Car"*. Technical Paper 2009-01-0778, SAE International, 2009. DOI: 2009-01-0778.

[13] A. F. Skea, P. R. Bullen, and J. Qiao. *"CFD Simulations and Experimental Measurements of the Flow Over a Rotating Wheel in a Wheel Arch"*. Technical Paper 2000-01-0487, SAE International, 2000. DOI: 2000-01-0487.

[14] R. H. Barnard. *"Road Vehicle Aerodynamic Design"*. MechAero, Hertfordshire, England, 3rd edition, 2015.

[15] J. N. Reddy. *"An Introduction to Continuum Mechanic"*. Cambridge University Press, Cambridge, UK, 1st edition, 2008.

[16] H. K. Versteeg and W. Malalasekera. *"An Introduction to Computational Fluid Dynamics"*. Pearson Prentice Hall, Edinburgh Gate, 2nd edition, 2007.

[17] Stephen B. Pope. *"Turbulent Flows"*. Cambridge University Press, Cambridge, UK, 3rd edition, 2001.

[18] Florian Menter. *"A New Generalized $k-\omega$ Model-Putting Flexibility into Turbulence Models (GEKO)"*. PowerPoint, 2018.

[19] ANSYS Inc. *"ANSYS Fluent Theory Guide"*, 2018.

[20] Teddy Hobeika, Simone Sebben, and Christoffer Landstrom. *"Investigation of the Influence of Tyre Geometry on the Aerodynamics of Passenger Cars"*. Journal Article 2013-01-0955, SAE International, 2013. DOI: 2013-01-0955.

[21] Mattias Olander. *"CFD Simulation of the Volvo Cars Slotted Walls Wind Tunnel"*, 2011.

[22] Emil Ljungskog. *"Investigations of Flow Conditions in an Automotive Wind Tunnel"*. PhD thesis, Chalmers University of Technology, 2017.

[23] Qui Z., L. Löfdahl, Landström C., and Josefsson L. *"Wheel Aerodynamic Developments on Passenger Cars by Module-based Prototype Rims and Stationary Rim Shield"*. In *FISITA Automotive World Congress*, 2010.

[24] Modlinger F. and Adams N. *"New Directions in the Optimization of the Flow around Wheels and Wheels Arches"*. In *7th MIRA International Vehicle Aerodynamics Conference*, 2008.

[25] Filipe Fabian Buscariolo and Kenneth J. Karbon. *"Comparative CFD Analysis Between Rotating and Static Cases of Different Wheels Openning Designs over a Performance Sedan"*. Technical Paper 2011-36-0271, SAE International, 2011. DOI: 2011-36-0271.

[26] Christoffer Landström, Tim Walker, Lasse Christoffersen, and Lennart Löfdahl. *"Influences of Different Front and Rear Wheel Designs on Aerodynamic Drag of a Sedan Type Passenger Car"*. Technical Paper 2011-01-0165, SAE International, 2011. DOI: 2011-01-0165.

[27] Henrik Berg and Adam Brandt. *"Investigation of Aerodynamic Wheel Design"*. Master's thesis, Chalmers University of Technology, 2018.

[28] Bradley D. Duncan, Satheesh Kandasamy, Khaled Sbeih, Todd H. Lounsberry, and Mark E. Gleason. *"Further CFD Studies for Detailed Tires using Aerodynamics Simulation with Rolling Road Conditions"*. Technical Paper 2010-01-0756, SAE International, 2010. DOI: 2010-01-0756.